

Time-Frequency Analysis of Experimental and Analytical Hub Loads of a Rotor Undergoing a Rotor Speed Change

Martin K. Sekula
Research Engineer
NASA Langley Research Center
Hampton, VA, USA

Carl R. Russell
Research Engineer
NASA Ames Research Center
Moffett Field, CA, USA

ABSTRACT

A two-part analytical study was conducted examining a small-scale, two-bladed rotor undergoing a change in rotor speed. First, a parametric study was conducted to understand how rotor transient response, determined using a time-marching solution, is affected by the choice of rotor wake model, blade elasticity, and inclusion of an elastic support structure model. The second part of the study compared results from an analytical model of the NASA Multirotor Test Bed (MTB) undergoing a rotor speed change to wind tunnel data. Since the analytical and experimental time histories were nonstationary signals, a Stockwell transform was employed to analyze the data in lieu of traditional Fourier transform-based methods. The analysis included extraction of time-varying frequency content of the rotor thrust and hub motion, damping ratios, instantaneous rotor speed, and instantaneous phase difference between thrust and hub motion. Use of a free wake model was found to be necessary to predict higher-harmonic thrust, however, it underpredicted the amplitude of the unsteady loads. Modeling the elasticity of the stiff rotor blades installed on the MTB resulted in minimal impact on the computed vibratory loads compared to a rigid blade model. The current analytical model of the MTB, including an elastic support structure, properly predicted the measured trends in the frequency content of the thrust.

NOTATION

t – time, sec
 z_f – vertical hub displacement, in
 F_z – vertical hub force, lb
 N_s – number of inflow states in dynamic inflow model
 $S()$ – Stockwell transform coefficient matrix
 α_s – rotor shaft angle, deg
 μ – rotor advance ratio
 ζ_f – support structure damping ratio
DST – discrete Stockwell transform
MTB – Multirotor Test Bed
RPM – rotations per minute
TFR – time-frequency representation
TnFR – time-normalized frequency representation

mechanical complexity of the control system by replacing blade pitch control, typically provided through a mechanical swashplate, with multiple electronic motor speed controllers. The primary goal of these motor speed controllers is to adjust the rotor thrust of each rotor and thereby change the vehicle attitude to achieve the desired thrust vector magnitude and orientation. The consequence of this trim approach is that, unlike traditional, constant-speed rotors where the vehicle is designed to avoid frequency coalescence between harmonics of the rotor speed and vehicle structural modes, vehicles that utilize rotor speed variation for primary flight control will almost certainly have to contend with frequency coalescence and resulting transient modal excitation.

Most of the analytical and experimental work performed to date on variable speed rotors has been conducted at constant rotor speeds and thus does not consider the transient response of the rotor system [1,2]. Slowed rotor research has also been limited to constant rotor speed analyses and experiments, while acknowledging the frequency coalescence challenges of such rotors [3,4].

INTRODUCTION

Improvements in electric powertrains, electronic controllers, and electric energy storage have led to rotor speed variation as the preferred method of flight control for small-scale, multi-rotor unmanned aerial vehicles. The use of rotor speed variation combined with a multirotor configuration simplifies the control laws required to trim the aircraft and reduces the

One example of analysis where rotor speed change is considered is the transient blade response during rotor startup and shutdown in shipboard and oil rig operations. Of particular interest is the large blade flapping response caused by low centrifugal loads combined with the turbulent aerodynamic environment of the landing pad (which can also include landing pad motion for shipboard operations). These

blade motions can lead to tunnel- and tail-strikes for tandem and traditional helicopters, respectively, and therefore, these analyses are more interested in maximum blade deflections and azimuth angle of occurrence than time-varying spectral content [5,6].

Recently, Mortimer [7] conducted an experimental study of a two-bladed, 1.108 meter rigid rotor (without flap or lag hinges) undergoing an 18% rotor speed change (900 to 1080 RPM) over three rotor revolutions. The experiment was conducted with the rotor operating at several values of thrust coefficient, adjusted via blade pitch, to determine if disk loading influences the rotor transient loads and wake formation, the latter being measured with particle image velocimetry. The study also included a computational fluid dynamics (CFD) analysis. Both the experiment and the analytical model agreed well and indicated that the rotor speed change did not result in a thrust overshoot; instead, the rotor smoothly transitioned from one steady thrust condition to another. The authors observed that the rotor torque underwent a substantial, 180% increase above the nominal torque during the rotor speed change. The CFD analysis concluded that the torque overshoot was due to inertial loads produced during rotor acceleration and not by the aerodynamic forces.

More recently, Chandrasekaran and Hodges [8] conducted an analytical study of an elastic rotor undergoing a rotor speed change and passing through resonance conditions. Their analysis of a large, 20-ft diameter rotor was motivated by the potential to improve rotor performance by changing the operational rotor speed – not by using the rotor speed for primary flight control. Their study examined the elastic blade response of the rotor when blade modes coalesce with multiples of blade passage frequencies. Due to the scale of their rotor, the rotor speed changed relatively slowly compared to small-to-medium-scale unmanned aerial vehicles. Their transient response study was conducted using DYMORE multibody analysis [9] and the aerodynamic model employed a finite-state inflow model. The frequency content of their rotor response was analyzed using a Fourier analysis on a subset of the time history instead of a true time-frequency analysis.

The present work is divided into three sections to methodically discuss the modeling and analysis of a rotor undergoing a rotational speed change. In the first section, several nonstationary signal analysis methods are reviewed and compared for application to rotorcraft loads analysis. One of these techniques, the Stockwell transform, is described in more detail and utilized throughout this work. In the next section, an analytical model of a rotor undergoing a rotor speed change is described. The model has been developed using the comprehensive aeroelastic rotorcraft analysis CAMRAD II [10]. This model is used in a parametric study to identify modeling assumptions (wake model, blade and support structure elasticity) that are important to the proper modeling of a small-scale (24.5 inch diameter) rotor

undergoing a rotor speed change. In the third and final section, the identified modeling requirements are utilized to develop an analytical model of a single-rotor configuration of the NASA Multirotor Test Bed wind tunnel model. A comparison of rotor vertical hub force experimental data and analytical results is conducted.

SIGNAL PROCESSING

Traditional signal processing assumes that the signal being analyzed is stationary – its frequency content is invariant as a function of time. This assumption is fundamental to all Fourier-based signal analysis methods such as the fast Fourier transform or the discrete Fourier transform. A Fourier analysis will not treat a transient signal as a temporally-localized event, but rather as harmonic content that is constant across the entire time interval being examined – a solution that may be mathematically correct, but not an instantaneous representation of the frequency content of the signal.

Nonstationary signals, signals where the frequency content changes as a function of time, require analysis techniques that temporally localize the frequency content. Nonstationary signal analysis is a mature signal processing discipline comprised of many methods and approaches [11]. Two of the more well-known examples of these signal analysis techniques are short-time Fourier transform (STFT) and continuous wavelet transform (CWT). STFT approach divides a signal into a series of time segments, within which the signal can be assumed to be quasistationary, yielding a series of spectra as a function of time. One of the major drawbacks of the STFT is that it involves a tradeoff between spectral and temporal resolution. Choosing a shorter time segment length increases the temporal resolution of the analysis, but simultaneously reduces the frequency resolution since fewer samples are used in the transform. This and other shortcomings can be mitigated using overlapping time segments and apodization functions, such as a Hamming window, to reduce spectral leakage.

The continuous wavelet transform is one of the most popular approaches to time-frequency analysis. The technique is quite versatile in its application partially because of the large number and types of mother wavelet functions, or basis functions [12]. The choice of basis function is dictated by the specific application. Therefore, the user must determine which function is appropriate for the analysis – improper choice of a basis function can result in the mischaracterization of the signal or nonsensical results. Unlike a Fourier transform, where the sinusoidal basis function is the same length as the entire signal, a CWT changes the scale (i.e., temporal length) of the mother wavelet. Adjusting the scale of the wavelet changes its apparent frequency – the smaller the scale, the higher the frequency. Temporal localization is achieved by translating the scaled wavelet across the entire signal. Some of the drawbacks to the CWT are: time-locally referenced phase (instead of a globally referenced phase), nonuniform distribution of voices (CWT equivalent of

frequency bins) that results in an oversampled representation of the low-frequency spectrum and undersampled representation of the high frequency spectrum, possible attenuation of high frequency signals, and no representation of the zero frequency [13].

In the present work, the nonstationary signal analysis is based on the S-transform [14], sometimes referred to as a Stockwell transform. This transform is already employed in a diverse range of applications such as medical diagnostics, seismology, and astrophysics [15,16,17,18]. The S-transform, Eq. 1, is similar in implementation to the CWT. It utilizes a Gaussian mother wavelet function, but this function is modified with a phase correction factor.

$$S(\tau, f) = \int_{-\infty}^{\infty} h(t) \frac{|f|}{\sqrt{2\pi}} e^{\frac{-(\tau-t)^2 f^2}{2}} e^{-i2\pi f t} dt \quad (1)$$

In Eq. 1, $h(t)$ is the signal time history, f is the frequency or voice of the S-transform, and t and τ are time in the time- and S-transform domain, respectively. The S-transform can also be rewritten in terms of a Fourier transform

$$S(\tau, f) = \int_{-\infty}^{\infty} H(\alpha + f) e^{\frac{-2\pi^2 \alpha^2}{f^2}} e^{i2\pi \alpha \tau} d\alpha \quad (2)$$

where H is the Fourier transform of $h(t)$ and α is the frequency in the frequency (Fourier) domain. This formulation is useful in developing a more efficient algorithm for computing the S-transform.

The S-transform has several advantages compared to CWT. First, the phase information calculated by the S-transform is absolutely referenced to $t = 0$, the initial time of the signal, thereby providing more meaningful phase information than a wavelet transform, whose phase is locally referenced. The amplitude response of the S-transform is frequency invariant, unlike a CWT, where the coefficient amplitude rolls off at higher frequencies or smaller scales. Furthermore, the S-transform is theoretically perfectly invertible. Lastly, averaging the S-transform in time collapses it into a Fourier transform of the signal, therefore the output of the transform is more easily interpretable, since it directly relates to a traditional Fourier transform [13,14].

In the present analysis, the discrete S-transform (DST) is employed to examine the time-varying frequency content of a rotor response due to a change in rotor speed. The DST equation, based on the S-transform in Eq. 2, is

$$S\left[jT, \frac{n}{NT}\right] = \sum_{m=-\frac{N}{2}}^{\frac{N}{2}-1} H\left[\frac{m+n}{NT}\right] e^{\frac{-2\pi^2 m^2}{N^2}} e^{\frac{i2\pi m j}{N}}, n \neq 0 \quad (3a)$$

where $H[\cdot]$ is discrete Fourier transform of N -point time series, $h[nT]$; T is the sample period; and j , m , and

$n = 0, \dots, N-1$ [13]. For $n=0$, the zero frequency, the DST is defined as

$$S[jT, 0] = \frac{1}{N} \sum_{k=0}^{N-1} h[kT]. \quad (3b)$$

Equation 3b highlights one of the drawbacks of the DST – it does not provide a time-localized mean value of the signal, just the overall mean for the time series. A separate approach is required to extract the local mean. In the present work, a constant sample length moving average is employed.

Another potential problem with the DST is the computational requirements. To analyze a signal of length N , the full DST calculates an $N \times N$ matrix of complex coefficients. For longer time histories, the computational cost may make the transform intractable due to both computational and memory requirements. In the present work, this issue is avoided by computing the transform for only a subset of the frequency range – limiting it to less than the user-selected maximum frequency of interest. This approach does not allow for a perfect inversion of the transform, since limiting the frequency range acts as a form of a low-pass digital filter. Furthermore, Eq. 3a implies that the DST produces a double-sided spectrum, but just as with the discrete Fourier transform, it can be reduced to a single-sided spectrum, thereby nearly halving the memory requirements.

To provide further insight into the differences between STFT, CWT, and S-transform analyses, wind tunnel data for a constant-rotor speed condition are analyzed using the three approaches. The data were acquired during the 2019 entry of the Multirotor Test Bed (MTB) at the U.S. Army 7- by 10-Foot Wind Tunnel at the NASA Ames Research Center [19]. A photograph of the testbed in the facility is provided in Fig. 1. The MTB is a reconfigurable wind-tunnel model capable of supporting the testing of up to six rotors at different rotor spacings with different rotor tilt and testbed pitch attitudes. The data and analysis presented in this work are for a single, 2-bladed rotor configuration. The rotor blades are commercially available KDE-CF245 blades. They have a radius of 12.25 inches, and are rigidly attached to the rotor hub, without pitch control.

Figure 2 presents a comparison of the rotor thrust time history analyzed using a STFT with two window lengths, CWT, and DST. The data were acquired at a free stream velocity of 40 ft/s, the rotor operating at 2000 RPM ($\mu = 0.187$), and a -5 degrees (nose-down) shaft tilt. The sampling rate was 4 kHz. The bottom of each subplot provides the thrust time history. Above the time history is a waterfall plot called a time-frequency representation (TFR). The TFR is a visualization of the transform where the abscissa represents time, the ordinate represents frequency, and the color intensity represents the magnitude of the transform coefficients. To the right of the waterfall plot is the FFT of the entire time history and the time-average of the transform spectrum. The axes of the FFT plot are transposed, compared



Figure 1. MTB installed in the U.S. Army 7- by 10-Foot Wind Tunnel at NASA Ames.

to standard convention, so the frequency is on the ordinate to match the waterfall plot.

Figures 2a-2b provide the TFRs of the rotor thrust determined using a STFT with a 256 sample (0.064 sec) and a 4096 sample (1.024 sec) window, respectively. For simplicity, these analyses were conducted without any window overlap or an apodization function. The 256-sample window length, Fig. 2a, shows more time dependence in the spectral content but resolution of the frequency content is coarse. The time average of this short-window STFT (red) envelopes the full time history FFT (blue). The longer 4096-sample window, Fig. 2b, significantly improves the frequency resolution of the spectral content, but at a cost of temporal resolution – there are only five windows spanning the entire time history. The longer windows did improve the comparison between the time-averaged STFT and the FFT of the full time history.

The TFRs of the rotor thrust determined by a CWT using a Morse wavelet and DST are provided in Figs. 2c-2d, respectively. Both TFRs of these two transforms show much higher temporal resolution than the STFT approach. Qualitatively, these magnitude waterfall plots appear similar, although the frequency range of the CWT is more limited than the DST's, 1473 Hz versus 2000 Hz. It should be noted that for the purposes of this comparison, the full DST spectral content is presented. The CWT analysis resulted in 115 voices (frequency bin equivalent in time-frequency analysis) representing the full spectral content, while the DST consists of 10299 voices – the same as the number of frequencies in a FFT of the full signal. The distribution of the CWT voices is indicated by the symbols on the time-averaged voice/FFT plot on the right side of the TFR in Fig. 2c. As discussed previously, the majority of the CWT voices are concentrated at the low frequency end of the spectrum with very few voices at higher frequencies. The time-average of the CWT voices envelope, and closely follow the FFT at low frequencies, but as the frequency increases, the average of the voices overpredicts the frequency content. On the other hand, the time-average of the DST is the FFT of the entire signal (red and blue traces match exactly). The DST also provides the

steady coefficient, which is cut off in this figure in order to highlight the fluctuating content.

ANALYTICAL MODEL

The comprehensive aeroelastic rotorcraft analysis CAMRAD II was used to simulate a single-rotor configuration of the MTB. The rotor consists of two commercially available KDE-CF245 blades attached to a rigid hub with a single fastener through the root of each blade. The blade lag motion is friction-restrained by this fastener. The blades are carbon-fiber composite with a radius of 12.25 inches and a mass of 34.9 grams per blade. The rotor does not allow for any blade pitch adjustment.

The blade structural properties were estimated based on the blade geometry and an experimentally determined cantilevered blade flap frequency of 71 Hz. The blade mass distribution was estimated based on the product of the local chord and airfoil thickness, with the material density adjusted until the analytical model blade mass agreed with the measured value. The sectional polar moment of inertia values were based on a formula given in the CAMRAD II manual for estimating structural dynamics properties of a rotor blade. Even though the blades are composite, due to their high stiffness and a lack of available detailed structural properties, they were treated as isotropic beams, with their stiffness properties loosely based on the DJI Phantom rotor blades [20]. The stiffness values were simultaneously adjusted until the first flap frequency matched the measured value. A fan plot limited to the first three modes for this rotor is provided in Fig. 3. The lowest-frequency mode, the flap mode, has a frequency of 75.6 Hz at a rotor speed of 1500 RPM and increases to 83.7 Hz at a rotor speed of 2500 RPM.

The aerodynamic loads were calculated using an 18-panel lifting line method and XFOIL-developed airfoil tables at four spanwise stations [21]. The effect of rotor inflow modeling on the transient rotor response was examined using three CAMRAD II inflow/wake models – a uniform inflow, free wake, and dynamic inflow. The uniform inflow model utilized the White and Blake linear inflow variation. The free wake consisted of a single tip vortex filament extending three revolutions from the rotor blade. The tip vortex core size of $0.05\bar{c}$ (where \bar{c} is the average chord length) was selected based on the rotor thrust [22] and used a Scully vorticity distribution with a square root vortex radius growth function. The dynamic inflow model was the CAMRAD II implementation of the Peters-He model.

A notional elastic support structure for the rotor was modeled using a single-mode modal representation. To further bound the scope of this study, the modal displacement was limited to the vertical degree of freedom. The mode was tuned to a natural frequency of 70 Hz, with a peak-to-peak displacement of 0.0015 inches for the rotor operating at 1500 RPM, -5 degree nose-down shaft tilt, and 40 ft/s free stream

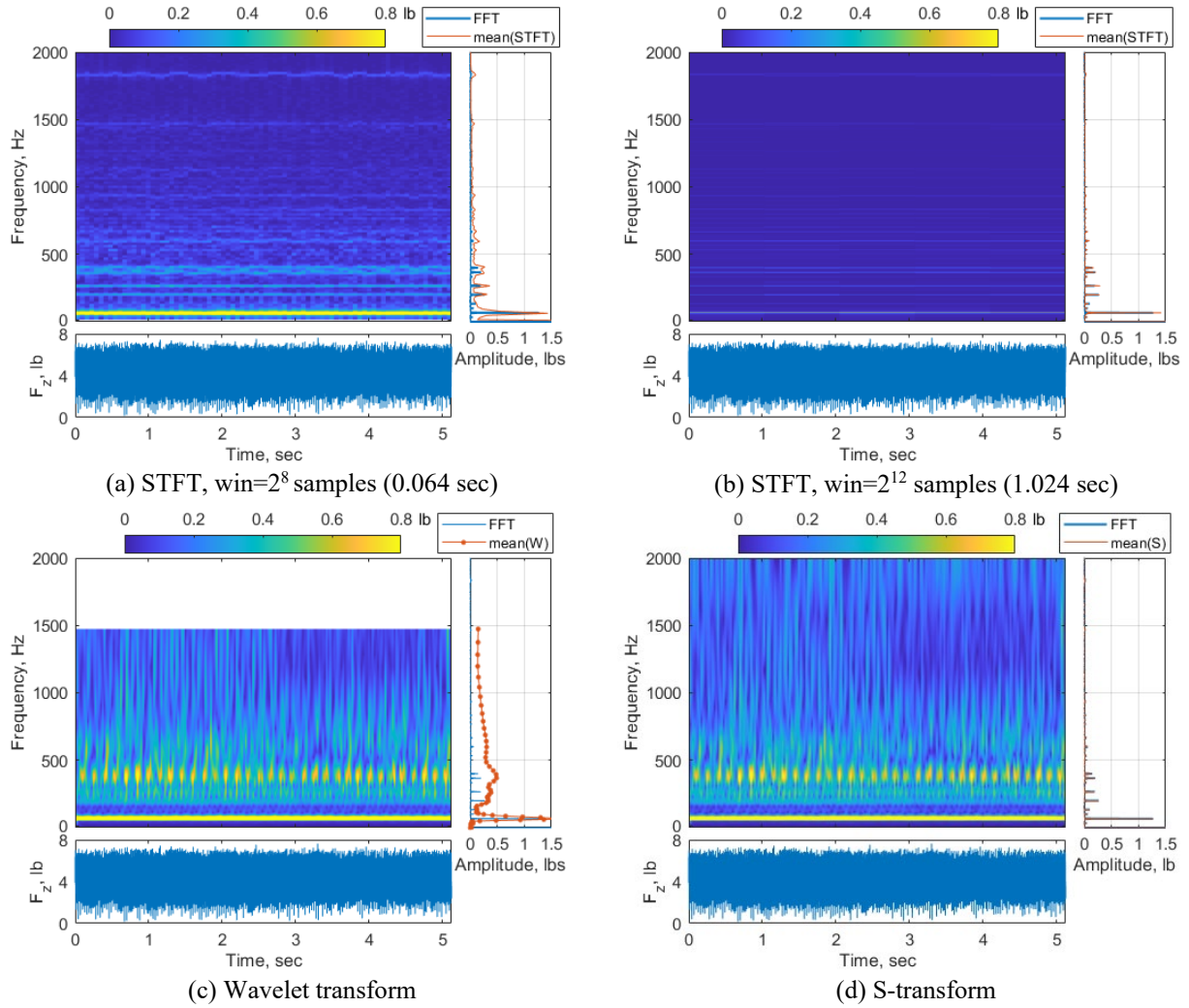


Figure 2. Comparison of STFT, CWT, and DST of rotor thrust for MTB rotor, $V=40$ ft/s, $\Omega=2000$ RPM, $\alpha_s=-5$ deg, 4000 Hz sample rate.

velocity. These frequency and displacement values were chosen to provide a 2P frequency crossing as the rotor speed changes from 1500 to 2500 RPM while limiting the support structure displacement.

The CAMRAD II solution procedure for a rotor speed variation problem is a two-step process. First, a periodic solution is calculated at the initial rotor speed. This solution is then utilized as the initial condition for the second step in the analysis where the rotor response is calculated using a time-marching solution with a piecewise continuous function defining the rotor speed as a function of time. The time integration approach utilized in this study is the linear Newmark method with a typical step size of 0.0002 seconds, or approximately 3 degrees, for a nominal rotor speed of 2500 RPM. This analysis assumes an ideal drive system where the rotor/motor inertia does not affect the ability of the motor to track the prescribed rotor speed. Therefore, motor torque limits that would typically constrain the rate of rotor speed change are not modeled [7]. Comprehensive analyses often assume the blades are identical, and the solution is based on an identical blade response with a phase offset used to account for blade azimuth differences. In the present analysis, the

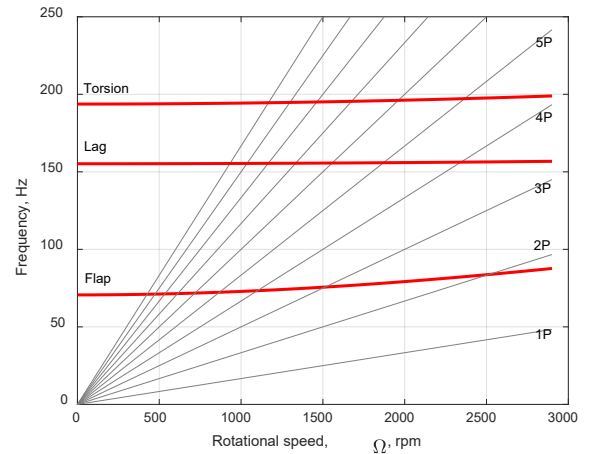


Figure 3. MTB rotor fan plot.

rotor speed changes during forward flight, thus invalidating the identical blade response assumption, and therefore requiring that the blade response be solved simultaneously for all blades.

The analytical model was validated by comparing the time-marching solution for a constant rotor speed case to experimental data. The experimental wind-tunnel data were acquired for a free stream velocity of 40 ft/s with a rotor speed of 2000 RPM, and a -5 degree nose-down shaft tilt – the condition examined using the time-frequency analyses presented in Fig. 2. The experimental steady thrust and torque values are compared in Table 1 to analytically-determined values for four aerodynamic models – uniform inflow, free wake, and 21- and 55-state dynamic inflow. The thrust of the uniform inflow and free wake cases agree well with the wind tunnel data. The dynamic inflow cases overpredicted the thrust by approximately five percent. All four models overpredicted the torque – approximately 15 percent for the uniform inflow and free wake, and 20 to 24 percent for the dynamic inflow. Since this study is limited to the rotor thrust, the analytical models are considered to be in general agreement with the experiment.

A comparison of the vibratory vertical hub force, F_z , is presented in Table 2. The table provides the first six harmonics of the vibratory force for the wind tunnel data and the four CAMRAD II cases compared in Table 1. The two dynamic inflow models produced 2P F_z vibratory loads that matched the experiment well, while the uniform inflow and free wake models underpredicted the 2P vibratory loads by approximately 75 percent. All four aerodynamic models underpredicted 4P vibratory loads – the 4P F_z amplitudes of the free wake and 55-state dynamic inflow models were the largest, but still only 65 and 74 percent of the experimental values, respectively. The free wake case was the only aerodynamic model to predict any appreciable 6P vibratory load, which was only 15 percent of the experimental amplitude. Possible sources of these differences may be aerodynamic modeling fidelity (such as airfoil tables), blade-to-blade differences that were not modeled or measured, wind tunnel phenomena, or the response of the MTB structure.

Table 1. Steady thrust and torque, experiment and CAMRAD II time-marching solution, $V=40$ ft/s, $\Omega=2000$ RPM, $\alpha_s=-5$ deg.

	Exp.	Uniform inflow	Free wake	Dyn. Inflow	
				$N_s=21$	$N_s=55$
F_z (lb)	4.40	4.37	4.37	4.63	4.62
M_z (ft-lb)	-0.312	-0.368	-0.354	-0.376	-0.387

Table 2. Vibratory vertical hub force (lb), experiment and CAMRAD II time-marching solution, $V=40$ ft/s, $\Omega=2000$ RPM, $\alpha_s=-5$ deg.

		1P	2P	3P	4P	5P	6P
Experiment		0.0486	1.27	0.0663	0.101	0.00151	0.267
Uniform		-	0.311	-	0.0133	-	0.00586
Free wake		-	0.317	-	0.0657	-	0.0402
Dyn.	$N_s=21$	-	1.30	-	0.028	-	0.00608
Inflow	$N_s=55$	-	1.22	-	0.0745	-	0.00377

A time-marching analysis of a rotor system undergoing a rotor speed change was conducted to understand how rotor system modeling can affect the results of a rotor speed change simulation. Three major components of the rotor system model were studied: rotor wake/inflow model complexity, blade elasticity, and support structure elasticity. The impact of each model component was assessed by performing a time-marching analysis where the rotor speed is varied. In all cases, the time-marching solution starts with a 1 second settling time, followed by a 1-second linear rotor speed change, and a constant rotor speed runout to produce a total time history of 5 seconds. The free stream velocity is 40 ft/s and the rotor shaft is pitched -2 degrees (nose-down). These parameters were selected to match MTB wind tunnel test conditions for a variable rotor speed test case. The initial rotor speed for this parametric study is 1500 RPM ($\mu=0.250$), while the final rotor speed is 2500 RPM ($\mu=0.150$). The rate of this rotor speed change was selected to minimize the computational effort by maintaining a relatively short time history.

The present study is focused on the rotor thrust, F_z . For each case examined, a DST of the 5-second time history is calculated. Figures 4a-4b provide a sample hub force time history and a TFR based on the DST of this time history, respectively. Added to the TFR is a gray dashed line identifying the frequency of the 2P harmonic as a function of time and a dash-dotted line identifying the 4P harmonic. In Fig. 4b, the 2P signal dominates the TFR, but also identifiable in the lower corners of the TFR are edge-effect artifacts that are more predominant at lower frequencies due to the larger time dilation of the S-transform basis function. These edge effects occur because the basis function extends beyond the end of the time history, making the spectral estimates less reliable.

The TFR can also be modified by normalizing the frequency using the instantaneous rotor speed, resulting in a “per revolution” representation of the time-varying spectrum. This time-normalized frequency representation (TnFR), presented in Fig. 4c, is more relatable to typical representations of rotor vibratory loads since each voice is related to a rotor harmonic (integer multiple and a fraction of) regardless of the instantaneous rotor speed. For brevity, throughout the remainder of this document any references to TFRs and TnFRs will imply that they are visualizations of the DST.

Inflow Model

The influence of the inflow model on the rotor vertical hub force, F_z , while undergoing a rotor speed change was assessed using four rotor inflow models: uniform inflow, free wake, 21-state dynamic inflow, and a 55-state dynamic inflow. The number of dynamic inflow states is based on the recent work by Chandrasekaran and Hodges for rotors operating at advance ratios of 0.2 and 0.3, respectively [8]. In order to isolate the effects of the aerodynamic modeling on the rotor loads, the rotor blades were modeled as rigid beams and the rotor was mounted on a rigid support structure.

The hub force time histories for these four cases and their TFR and TnFR are presented in Figs. 4–7. All four cases indicate the presence of a dominant 2P harmonic typical for a 2-bladed rotor. A prominent 4P signal is present in the free wake and the 55-state dynamic inflow cases, while the 21-state dynamic inflow model exhibits a small 4P load. The free wake case also exhibits a temporary 6P force during rotor speed increase that is not produced by the other models. This higher frequency content may be of particular importance for modeling the response of higher-frequency structural modes.

It should be noted that none of the four cases displayed a transient thrust when transitioning from the accelerating to constant rotor speed. This lack of a transient response, such as an overshoot, may be due to the lack of a drivetrain and control system model, but this observation is consistent with experimental results by Mortimer [7] who noted that a thrust overshoot was absent from their data.

A more quantitative assessment of the vibratory environment due to the various aerodynamic models can be made by examining the per-revolution voice amplitudes extracted from the TnFR of the vertical hub force. The 2P and 4P S-transform amplitudes, and the moving-mean thrust, calculated using a 0.1 second moving window, are presented in Fig. 8. The moving-mean thrust, Fig. 8a, calculated using the uniform inflow and free wake models track well with one another. The dynamic inflow models produced higher thrust values, with the 21-state model resulting in larger thrust than the 55-state model. This trend in thrust as a function of the number of states is an indication that more than 21 states are needed to properly model the aerodynamic environment for this case; thrust convergence in dynamic inflow models is from “above” as the number of states is increased [23]. Additional analysis with the number of inflow states as high as 88 (not presented) resulted in minor changes to the mean and vibratory thrust, indicating that the model is sufficiently converged with 55 states.

The 2P and 4P vertical hub force amplitudes for the four cases are presented in Figs. 8b–8c, respectively. The 2P loads at the initial 1500 RPM show a significant scatter between the four cases. The 21-state dynamic inflow model results in a significantly larger vibratory load than the other three cases. These larger loads may be due to an insufficient number of

states, as discussed previously. The remaining three aerodynamic models result in similar 2P amplitudes for the vibratory hub force at this initial rotor speed. As the rotor speed is increased, the uniform inflow and the 55-state dynamic inflow models result in a small increase in the 2P vertical hub force amplitude, while the 2P vibratory hub force of the free wake model appears to be insensitive to the rotor speed change. The 4P vibratory loads are insensitive to rotor speed for the uniform inflow model, Fig. 8c. The dynamic inflow models both indicate a decrease in 4P vibration with increasing rotor speed, which is contrary to the free wake model that indicates an increase in 4P vibration with increasing rotor speed.

The source of the limited sensitivity to the 2P hub force can be inferred from the blade equations of motion and by examining the rotating frame blade root vertical shear. The current rotor consists of two blades, modeled as rigid beams that are restrained at the root from any articulation (hingeless and bearingless). Therefore, the blade equations of motions lack velocity or acceleration terms (except for the rotation of the rotor), and the only contribution to the out-of-plane dynamic loads is due to azimuth-related changes in the aerodynamic loads. Since the only blade motion is the rotation about the rotor shaft, the aerodynamic terms in the equations of motion are only affected by the local differences in angle of attack (due to inflow and tangential velocity variation) and dynamic pressure. The effect of these limitations on the blade dynamics can be seen in the rotating-frame blade root vertical shear force. The 1P, 2P, and 3P amplitudes of the blade root vertical shear force (based on the DST of the time histories, not presented) is provided in Fig. 9 for the uniform inflow, free wake, and 55-state dynamic inflow cases. In all three cases, the 1P amplitude of the blade root shear (red traces) almost doubles as the rotor speed increases from 1500 to 2500 RPM, while the amplitude of the 2P shear (black traces), the primary contributor to the 2P vertical hub force, is mostly insensitive to the change in rotor speed for all three cases. Also of note is that the free wake case is the only one that shows an appreciable change in the 3P amplitude of the vertical shear (green traces) as a function of time and rotor speed. The source(s) of this difference was not conclusively identified, but the more complex geometry of the off-body circulation of the free wake model is a likely source.

Blade Elasticity

The second modeling component examined was blade elasticity of this small-scale rotor and its impact on rotor vibration and dynamics. The analytical study of the elastic blade model was conducted using three aerodynamic models: uniform inflow, free wake, and 55-state dynamic inflow. The 21-state dynamic inflow model was not included in this study since one of the conclusions from the preceding section is that 21 states are insufficient to properly model the inflow during the rotor speed change.

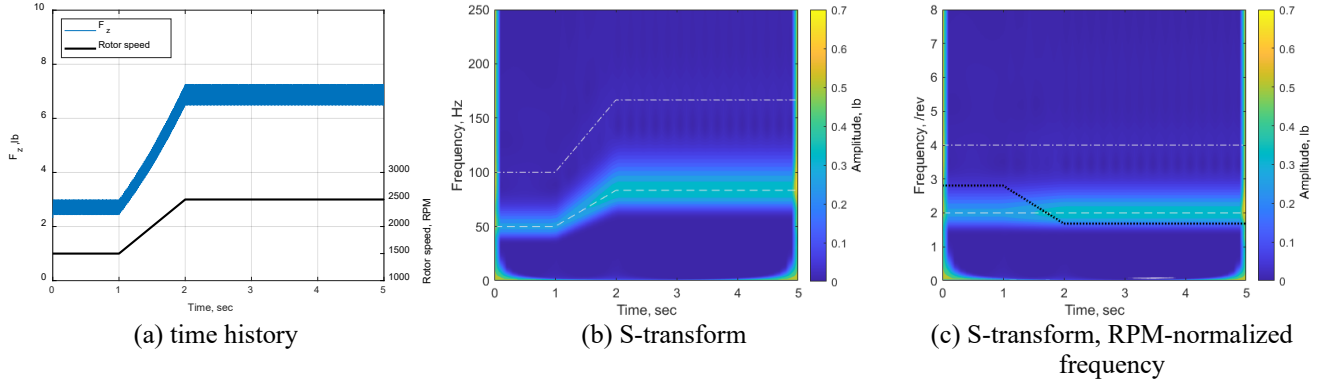


Figure 4. Hub vertical force and its TFR and TnFR; uniform inflow, rigid blades, rigid support.

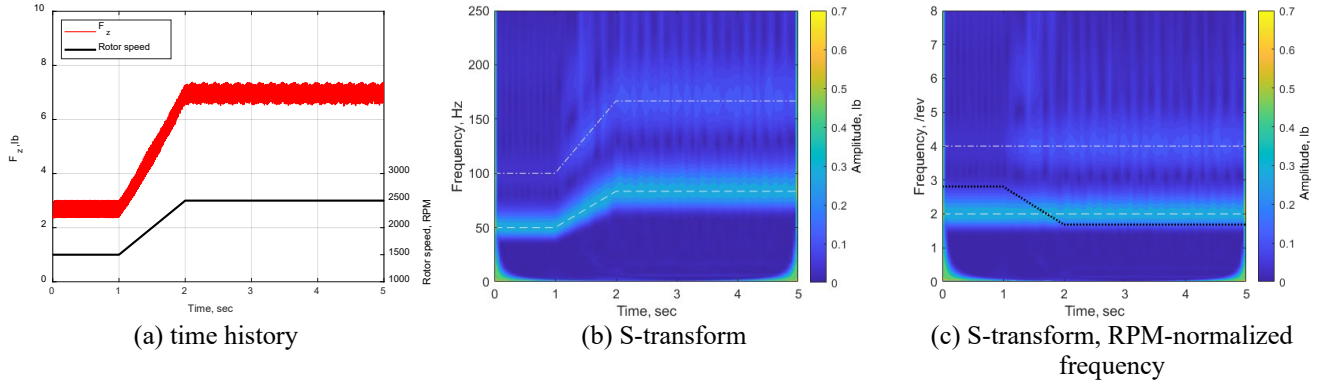


Figure 5. Hub vertical force and its TFR and TnFR; free wake, rigid blades, rigid support.

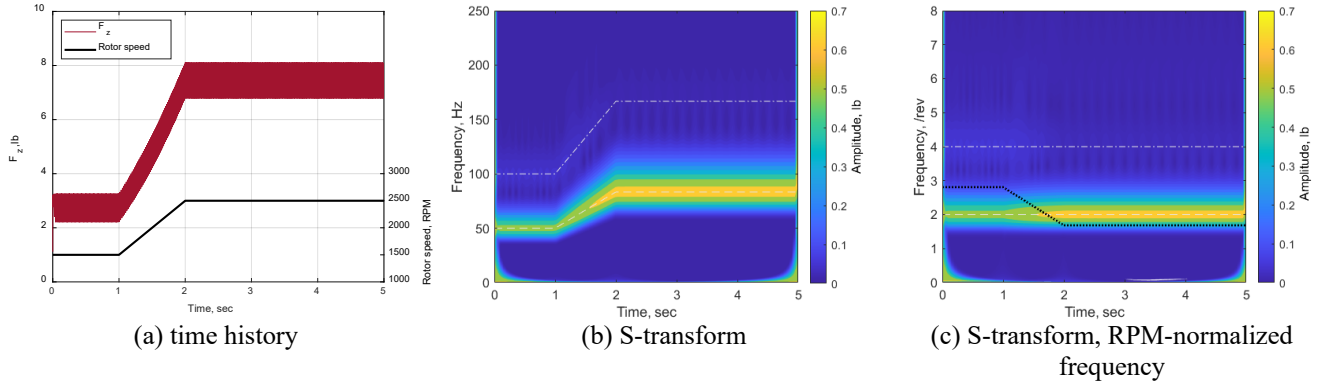


Figure 6. Hub vertical force and its TFR and TnFR; 21-state dynamic inflow, rigid blades, rigid support.

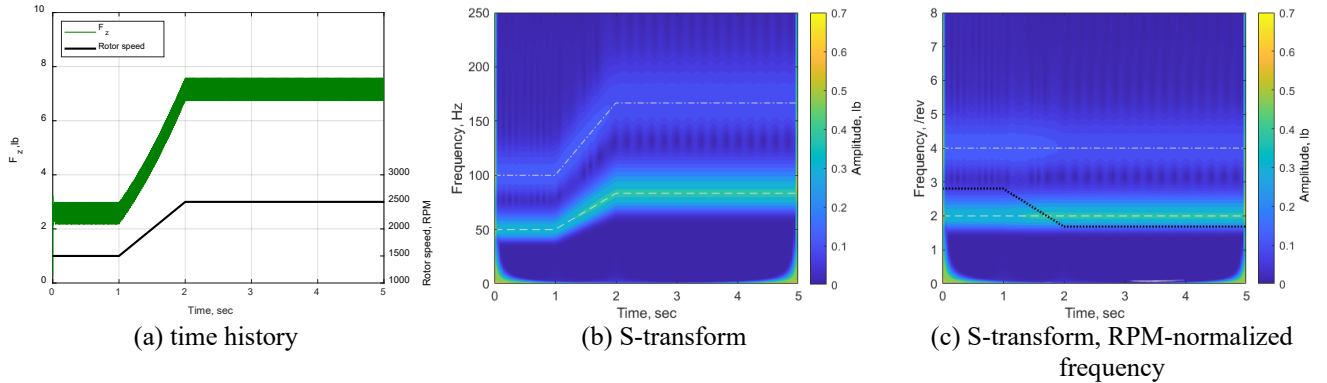


Figure 7. Hub vertical force and TFR and TnFR; 55-state dynamic inflow, rigid blades, rigid support.

Inclusion of blade elasticity in the current rotor model did not result in a significant difference in the rotor loads. The vertical hub force time histories and TFR did not show

notable differences compared to the rigid blade case (not presented). The moving mean, the 2P and 4P voice amplitudes of the DST for the three elastic blade cases are

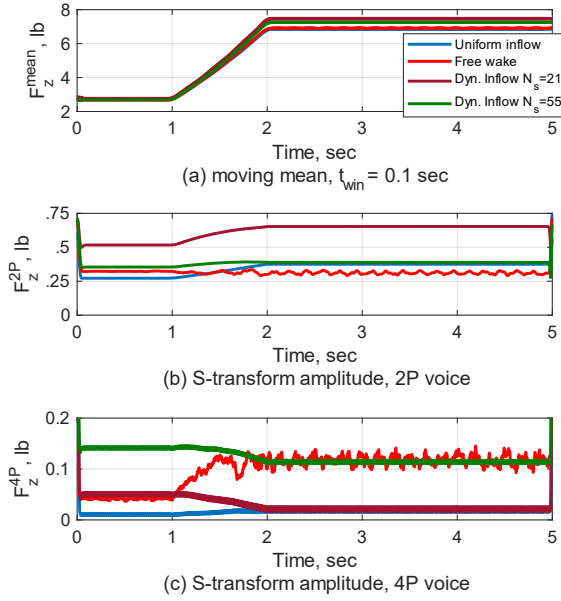


Figure 8. Hub vertical force; moving mean, 2P and 4P DST voices.

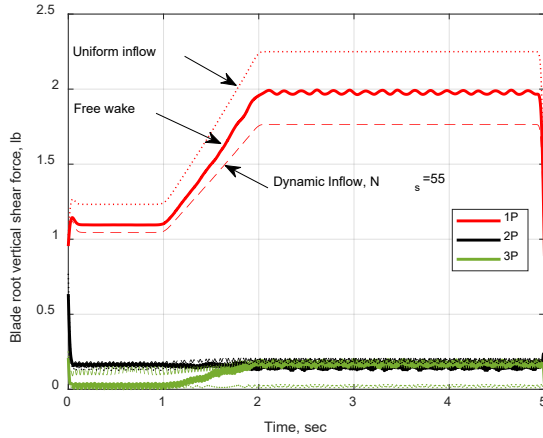


Figure 9. Blade root vertical shear amplitude (rotating frame); 1P, 2P and 3P TnFR voices.

provided in Fig. 10. For comparison, the rigid blade cases (presented in Fig. 8) are included in this figure as lighter traces. The plots indicate very minor differences in amplitudes. This insensitivity of the hub force amplitude to blade elasticity is due to the high stiffness of the blades.

Elastic Support

The final modeling component examined is the support structure elasticity, modeled as a notional 1-DOF (vertical direction) modal representation. Just like the elastic blade study, the analysis of the model that includes an elastic support structure was conducted using three aerodynamic models: uniform inflow, free wake, and 55-state dynamic inflow. The vertical hub force, F_z , due to the rotor speed change for the three aerodynamic models and an undamped support structure are provided in Figs. 11 - 13. These figures

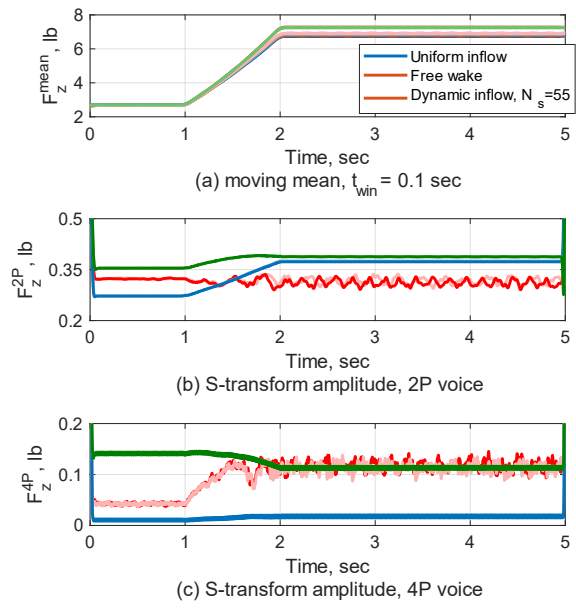


Figure 10. Hub vertical force time history moving mean, 2P and 4P TnFR voices; elastic blade, rigid support.

include the TFRs and TnFRs of the time histories. The black dotted line included in the TFRs and TnFRs highlights the 70 Hz frequency of the support structure mode. Following the previously defined format, the 2P harmonic is highlighted by a gray dashed line and the 4P by a gray dash-dotted line in these figures.

All three vertical hub force time histories (Figs. 11a-13a) exhibit an increase in the vibratory loads as the rotor speed increases and the 2P harmonic passes through a resonance condition at 1.6 seconds, 70 Hz (2100 RPM), followed by a decay of the vibratory loads as the rotor continues to the final rotor speed of 2500 RPM. Qualitatively, the dynamic inflow model produces the largest increase in vibratory loads, and the free wake model produces the smallest.

The TFRs and TnFRs, Figs. 11b-11c to 13b-13c, provide the time-varying frequency content of the vertical hub forces calculated with the three aerodynamic models. As noted in the aerodynamic model study with a rigid support structure, the uniform inflow model primarily produces 2P loads, while the free wake and dynamic inflow models additionally include 4P loads. Finally, the free wake also produces a short 6P vibratory force during the rotor speed change, consistent with the previous results. The elastic support structure introduces additional frequency content in the vertical hub force at 70 Hz as the frequency of the 2P harmonic approaches the support structure modal frequency, thereby exciting this structural mode. Once past the resonance condition, the 2P forces produced by the rotor continue to increase in frequency with increasing rotor speed, leaving the excited support structure mode to decay at its modal frequency of 70 Hz.

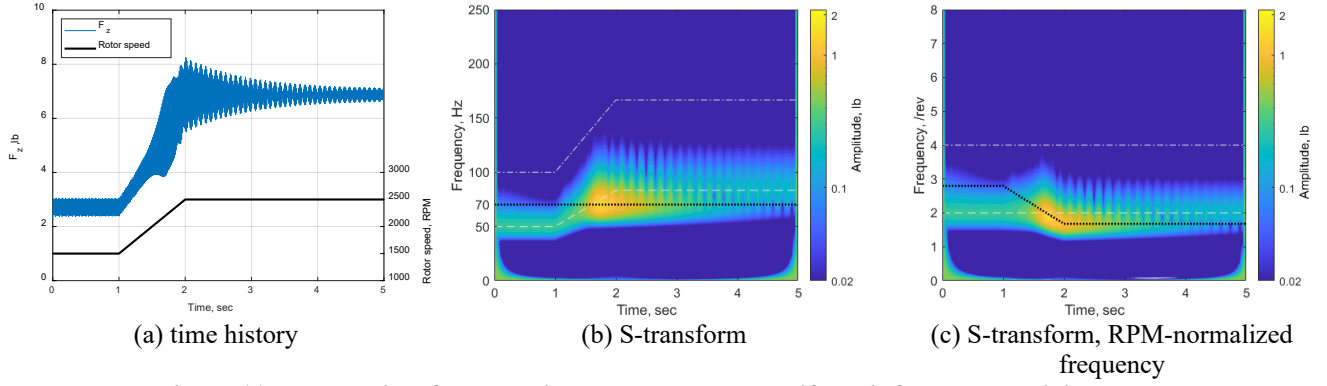


Figure 11. Hub vertical force and its TFR and TnFR; uniform inflow model, rigid blades, elastic support structure, $\zeta_r = 0$.

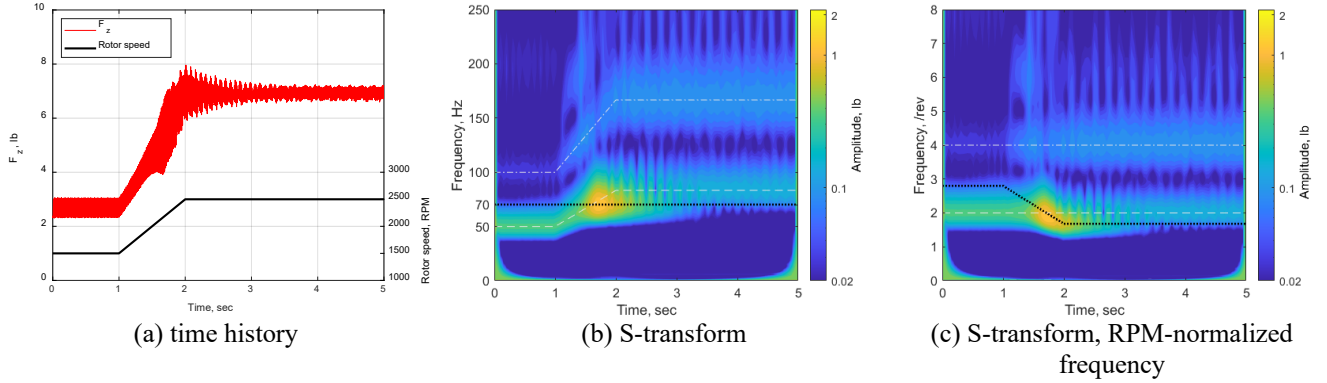


Figure 12. Hub vertical force and its TFR and TnFR; free wake model, rigid blades, elastic support structure, $\zeta_r = 0$.

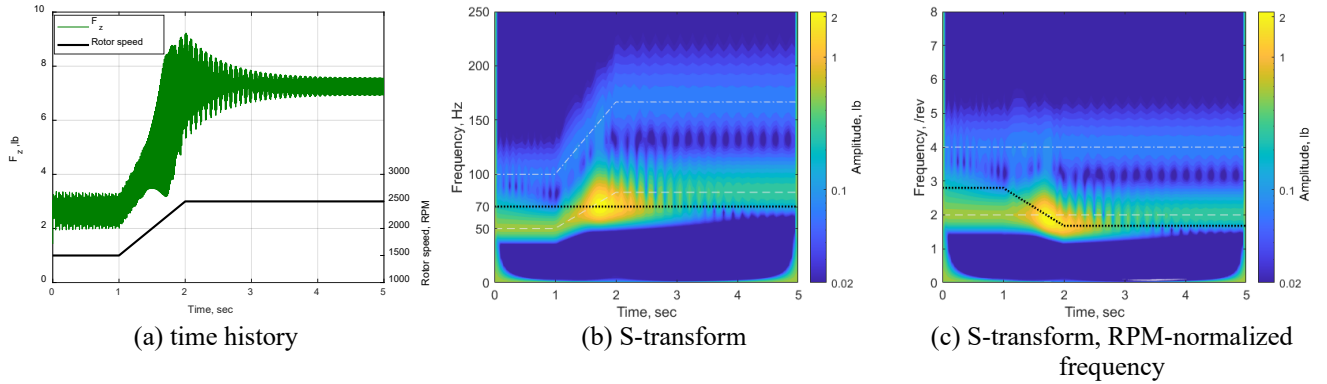


Figure 13. Hub vertical force and its TFR and TnFR; 55-state dynamic inflow model, rigid blades, elastic support structure, $\zeta_r = 0$.

The amplitudes of the 2P voice (from the TnFR) and the 70 Hz voice (from the TFR) were extracted from Figs. 11b-11c to 13b-13c and are provided in Fig. 14. Focusing on just these voices provides a clearer picture of the impact of the aerodynamic models on the 2P and 70 Hz vertical hub force (Figs. 14a - 14b, respectively) as the rotor passes through the resonance condition. All three cases show an exponential increase in 2P vibratory loads as the rotor speed increases and passes through resonance at 1.6 seconds and continue to increase for another 0.1 seconds. The peak amplitude for the uniform inflow case (blue trace) was 4.8 times the amplitude for 1500 RPM, while the free wake (red trace) and dynamic inflow (green trace) models increased 3.4 and 4.25 times their 1500 RPM amplitude, respectively. All three then decay to

new steady-state amplitudes corresponding to a steady-state 2500 RPM rotational speed. The 70 Hz voice amplitudes (Fig. 14b) follow the same trends, but the peak amplitudes of the DST for this voice are 4 percent (free wake) to 5 percent (dynamic inflow and uniform inflow) higher than the peak values for the corresponding 2P voices.

The vertical hub displacements generally follow the same trends as the corresponding vertical hub forces (Figs. 11-13). For brevity, only the time histories of the displacements (without the TFRs and TnFRs) for the three models are provided in Fig. 15. The moving mean (using 0.1 second window) of these time histories, the 70 Hz TFR voice and 2P TnFR voice of the hub deflection are presented in Fig. 16. For

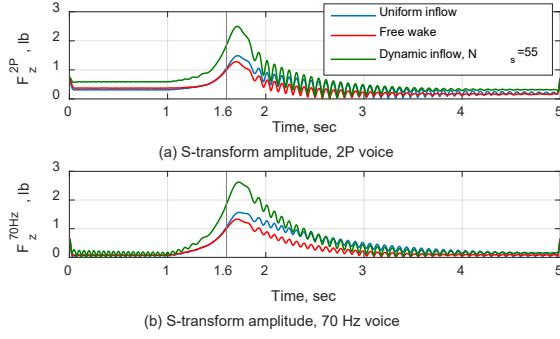


Figure 14. Hub vertical force DST amplitude as a function on time, 2P TnFR voice and 70 Hz TFR voice; rigid blade, elastic support structure, $\zeta_r = 0$.

all three aerodynamic models, the moving mean, Fig. 16a, shows that the increase in thrust from approximately 2.7 lb. (1500 RPM) to 6.9 lb. (2500 RPM) results in less than a 0.01 inch quasi-steady elastic deflection. The 2P dynamic response (i.e., 2P voice), presented in Fig. 16b, grows as the rotor speed approaches and passes through resonance at 2100 RPM (1.6 seconds, 70 Hz) resulting in amplitudes that are larger than the change in the quasisteady elastic deflection. All three cases indicate that the 2P vertical hub motion keeps increasing even after the 2P harmonic passes through 70 Hz. In all cases, the maximum amplitude is reached at approximately 1.73 seconds (2230 RPM) where the amplitudes are almost doubled compared to the amplitudes at 1.6 seconds. This time lag between when the rotor speed passes through resonance and the maximum response of the system is dependent on the rate of rotor speed change (not shown), with higher rates of rotor speed change decreasing the time lag and the maximum amplitude. Examining the 70 Hz voice, associated with the modal frequency of the support structure, Fig. 16c, indicates that the response of the rotor hub at this modal frequency follows a similar trend to the 2P voice, but the maximum amplitudes of the deflections are consistently 4 percent higher than the 2P voice maximum amplitudes, reflecting the observations made for the vertical hub force in Fig. 14.

These voice amplitudes can also be used to determine the damping of the rotor-support structure system. The damping ratio of the 2P and 70 Hz voices for the three cases are provided in Table 3. The 2P voice damping ratio is based only

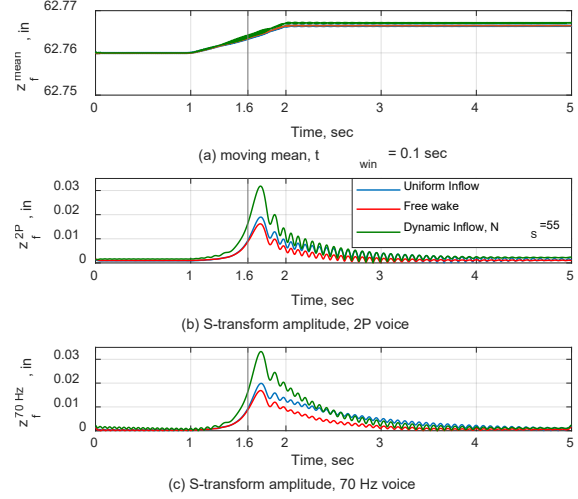


Figure 16. Hub vertical displacement, local mean, 2P TnFR voice and 70 Hz TFR voice; rigid blade, elastic support structure, $\zeta_r = 0$.

on the 2500 RPM portion of its record to maintain a constant frequency for the response. The aerodynamic damping of the 2P harmonic of this small-scale rotor in a pure plunge motion is small, 0.15 to 0.2 percent critical, depending on the aerodynamic model. For the 70 Hz voice, the natural frequency of the support structure, the aerodynamic damping is slightly higher, with damping ratio values of 0.2 to 0.35 percent critical, even though the support structure is undamped. These damping ratios were confirmed using more traditional logarithmic decrement and moving block methods.

Table 3. Percent critical damping ratio based on DST of hub displacement, $\zeta_r = 0$.

voice	Uniform inflow	Free wake	Dyn. inflow $N_s=55$
2P	0.15	0.22	0.22
70 Hz	0.23	0.36	0.36

The effect of structural damping on the rotor-support structure system was also examined. The modal damping of the support structure was set to 0.5 percent critical and a time-marching solution using the free wake model was obtained. The DST of the vertical hub force time history (not presented, due to qualitative similarity to Fig. 12) was used to determine

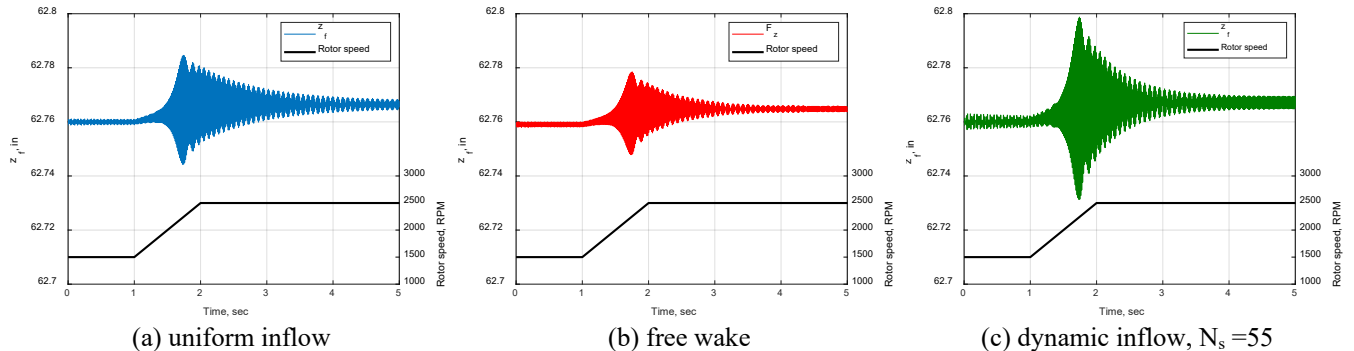


Figure 15. Hub vertical displacement time histories; rigid blades, elastic support structure, $\zeta_r = 0$.

the 2P harmonic amplitudes. These time-dependent 2P vertical hub force amplitudes (depicted as solid blue lines) are presented in Fig. 17. They are compared to the undamped elastic support structure model (solid red lines, previously presented in Fig. 14a.) Constant-rotor-speed periodic solutions were also determined for these two models spanning the 1500 to 2500 RPM rotor speed range in 50 RPM intervals. The results of these periodic solutions are included in Fig. 17 as symbols with colors matching their time-marching solution counterparts. Since the abscissa in Fig. 17 denotes time for the time-marching solution, the 2P amplitudes for each rotor speed from the periodic solution are plotted at the times corresponding to the same rotor speed in the time-marching solution. A secondary abscissa is included to denote the rotor speed.

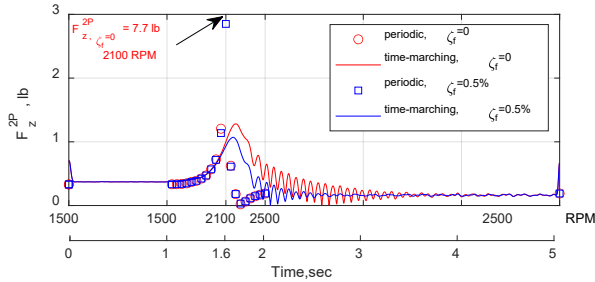


Figure 17. 2P hub vertical force response as a function of RPM; free wake, rigid blade, elastic support structure.

Comparing the time-marching solution for the damped support structure (blue line) to the undamped case (red line), the peak 2P amplitude (Fig. 17) decreased by 16 percent and occurs slightly sooner than the undamped case (0.075 seconds vs. 0.094 seconds after passing through resonance at 2100 RPM, 1.6 sec). As expected, the damped case transient force amplitude decays faster than the undamped case at 2500 RPM. The more interesting comparison of 2P hub loads is between the periodic and time-marching solutions. The maximum amplitudes of the periodic solutions for both the damped and undamped cases occur at 2100 RPM, the rotor speed at which the 2P harmonic crosses the modal frequency of the support structure (70 Hz). The peak amplitude of the periodic solution for the damped structure case is almost 3 times higher than the time-marching solution (2.85 lb. vs. 1.07 lb). For the undamped structure case, the peak amplitude

difference is even larger, 7.67 lb. for the periodic solution, vs. 1.28 lb. for the time-marching solution. It should be noted that while there is no structural damping in this case, the overall coupled rotor-support structure system does include some aerodynamic damping (see Table 3), thereby limiting the maximum response of the system. The other notable observation is that after passing through resonance, the 2P hub loads based on a periodic solution are significantly lower than the time-marching solution until the transient response decays.

The damping ratios for the damped support structure case, presented in Table 4, were determined using the 2P and 70 Hz voices from the DST of the hub motion (not presented). The damping of the 2P voice was unchanged compared to the undamped support structure case (compare Tables 3 and 4), while the 70 Hz voice damping was increased, reflecting the addition of the modal damping in the support structure model.

Table 4. Percent critical damping ratio based on DST of hub displacement, $\zeta_f = 0.5\%$.

voice	Free wake
2P	0.20
70 Hz	0.53

Additional insight into the coupled rotor-support structure dynamics can be obtained by determining the phase between the aerodynamic component of the vertical hub force and the hub motion by conducting a localized cross-spectral analysis using the DST [24]. This analysis is similar to a Fourier cross-spectral analysis, where the two signals are transformed into the frequency domain and a product of the first signal with the complex conjugate of the second signal is calculated. The localized cross-spectral analysis using the DST follows the same approach, but the elementwise product of the two DSTs is calculated. Calculating the complex argument of the DST product provides the localized (in time and frequency) phase between the two signals.

Again, for brevity, only the free wake cases will be examined. The cross-spectral amplitude and phase TFRs for the undamped support structure case are provided in Fig. 18. The amplitude TFR (Fig. 18a) indicates that the rotor hub motion

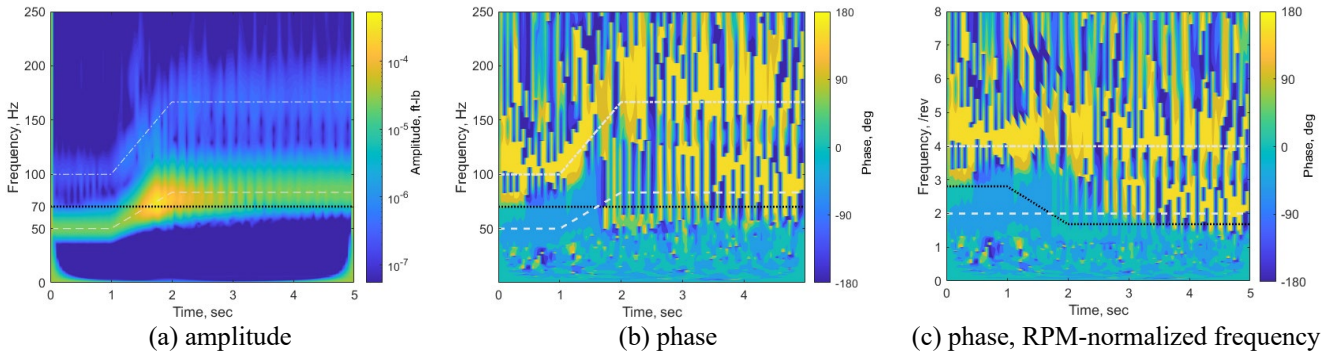


Figure 18. Amplitude and phase of localized cross-spectral analysis of the thrust and hub vertical displacement; free wake model, rigid blades, elastic support structure, $\zeta_f = 0$.

corresponds to excitation from the 2P, 4P and 6P aerodynamic forces. More insightful than the amplitude is the phase between the vibratory thrust and the hub motion, provided in Figs. 18b-c. On the surface, the phase appears to be random in nature, except for the first 1.5 seconds near the 2P harmonic where the phase appears to remain constant at 0 degrees.

To better understand how to interpret the phase TFR, its 2P voice is extracted from Fig. 18c and plotted with the rotor vertical hub force and rotor hub displacement in Fig. 19. In this figure, the total (aerodynamic and inertial) vertical hub force time history is provided in red in Fig. 19a, while the aerodynamic component of this force is provided in gray. Both at the starting and ending rotor speed, the vertical hub force primarily consists of aerodynamic forces. Only when the rotor speed is in the vicinity of the 2P resonance condition at 1.6 seconds, do the inertial forces become more dominant. This increase in inertial forces is due to an increase in hub motion, provided in Fig. 19b. The 2P phase as a function of time is provided in red in Fig. 19c. At the initial rotor speed of 1500 RPM, the phase between the rotor thrust and the hub motion is approximately 0 degrees. As the rotor speed approaches 2100 RPM at 1.6 seconds, the phase begins to change, and once it passes through 2100 RPM, the phase quickly reaches -180 degrees. The phase continues to change and wrap around until approximately 3.5 seconds, where the phase settles into small perturbations about -180 degrees (for clarity, the 2P phase was unwrapped for time > 3.5 seconds, to eliminate the 360 degree phase jumps between +/- 180 degree values). The unwrapped phase, presented in Fig. 19d, provides a clearer indication of how long the phase continues to change after the 2P harmonic passes through the resonance condition. The phase keeps changing for another 1.875 seconds after resonance, or almost 1.5 seconds after the final rotor speed is reached – corresponding to the length of time it takes for the transient response to decay in Fig. 19b.

The rotor-support structure model was also examined using a constant rotor speed periodic solution typically employed in rotorcraft analyses. The phase from this analysis is presented in black in Figs. 19c-19d. It differs from the time marching solution since it does not model the transient response of the system. In the case of the periodic solution, the rotor thrust and hub motion are in phase until the resonance condition is reached, then quickly shifts to -180 degree out-of-phase motion once the frequency of the 2P harmonic is higher than 70 Hz, the modal frequency of the support structure. This behavior is similar to a lightly-damped 1-DOF spring-mass-damper system with an external excitation force, making it a good analogy – the rotor, in this case, is a monolithic structure (blades are rigid, without articulation, representing the mass) attached to a modal representation of 1-DOF elastic structure (the spring), while the aerodynamic loads provide both the excitation force and the aerodynamic damping.

The vertical hub force time history, the hub displacement time history, and the 2P phase for a damped support structure model are presented in Fig. 20. The total vertical hub force

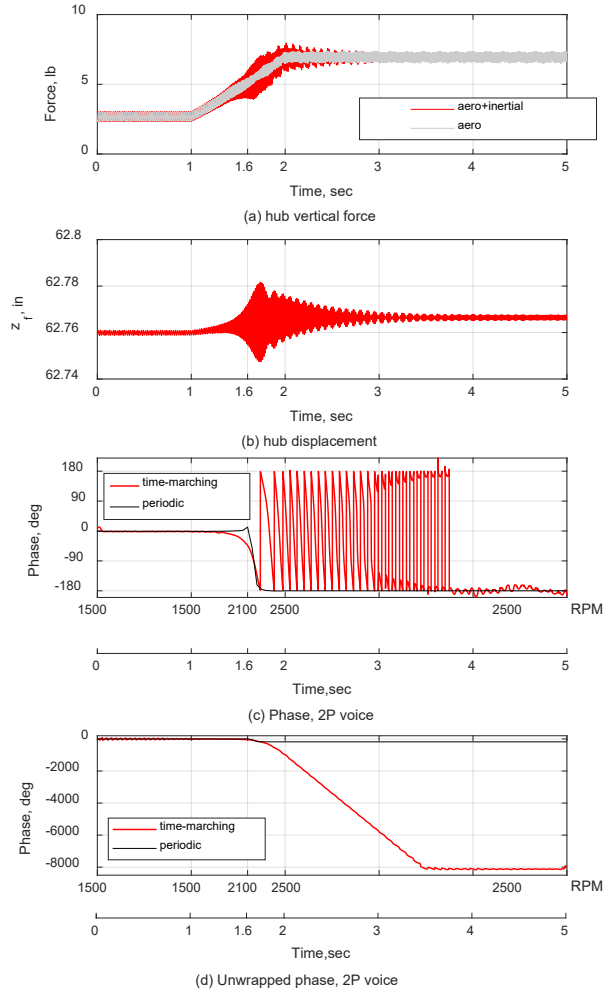


Figure 19. Vertical hub force and displacement and the phase of 2P time-marching and periodic solutions; free wake model, rigid blades, elastic support structure, $\zeta_r = 0$.

(blue line) and its aerodynamic component (gray line) are presented in Fig. 20a. Again, for the constant rotor speed portions of the time histories, the aerodynamic component makes up most of the vertical hub force. The inertial loads only become significant near the resonance condition, but as expected for a damped system, they are smaller than the undamped case due to the decrease in the hub motion (compare Fig. 19a to Fig. 20a. and Fig. 19b to Fig. 20b.)

The phase between the vertical hub force and the vertical hub displacement for the 2P harmonic is represented by blue lines in Figs. 20c-20d. For comparison, the phase of the periodic solution (black line) for the same rotor-support structure model is included in these figures. The wrapped phase, presented in Figs. 20c, provides a clearer indication of the difference in phase near the resonance condition for the two solution methods (time-marching vs. periodic). The phase of the periodic solution looks similar to its counterpart in the undamped structure case, Fig. 19c, but the change from 0 degrees to -180 degrees occurs over a wider range of rotor speeds, confirming the appropriateness of the 1-DOF mass-

spring-damper system analogy. The phase of the time-marching solution is also changed when compared to the undamped case. The phase change begins earlier than the undamped case, and it reaches the final phase of -180 degrees sooner since the transient response decays more quickly for the damped model. The unwrapped phase, Fig. 20d, is more useful for comparing to the phase of the undamped support structure model, included in red for convenience. Figure 20d indicates more clearly that the damped support structure phase reaches its final phase value sooner compared to the undamped structure. At the same time, Fig. 20d indicates that the rate of the phase change is the same for both the damped and undamped cases.

EXPERIMENTAL-ANALYTICAL MODEL COMPARISON

During the first wind-tunnel entry of the MTB, data was acquired for a single rotor configuration, where the rotor underwent a rotational speed change from 1500 to 2500 RPM as a proof of concept for acquiring transient rotor response

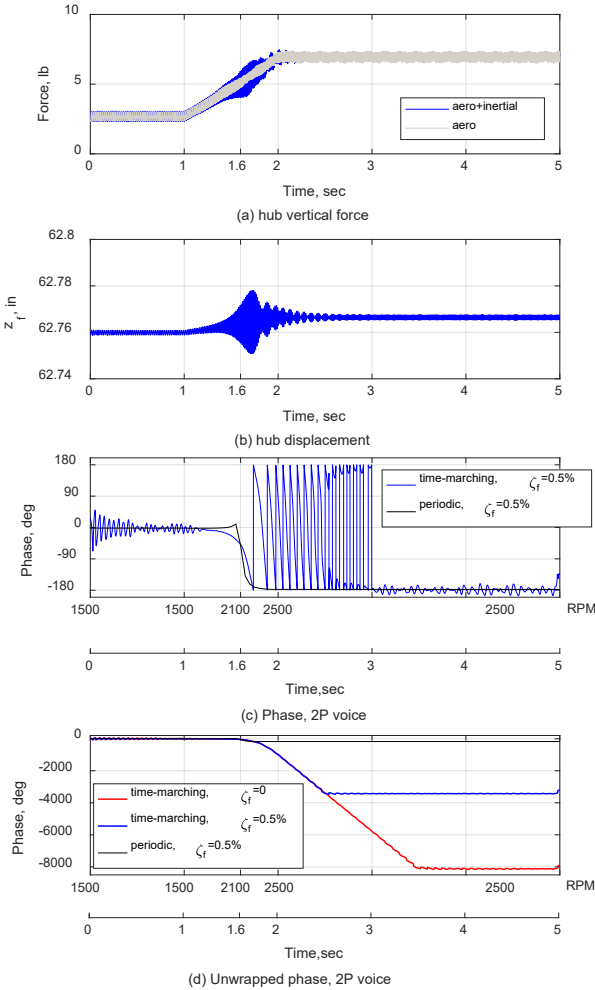


Figure 20. Vertical hub force and displacement and the phase of 2P time-marching and periodic solutions; free wake model, rigid blades, elastic support structure, $\zeta_r=0.5\%$.

data [19]. The rotor speed control was closed-loop but the gains were not tuned to provide a specific rate of change. The free stream velocity for this case was 40 ft/s with the testbed pitched -2 degrees (nose down). The experimentally acquired rotor vertical force time history and its TFR and TnFR are presented in Fig. 21. Because the rotor speed was not measured in a time-correlated manner and updated every 0.7 sec (while the hub force was acquired at 4 kHz), the rotor speed was estimated by identifying the time-dependent peak amplitude of the DST in the 40 to 100 Hz frequency range and assuming that the peak amplitude defines the 2P signal of the rotor hub force. This peak amplitude was used to determine the instantaneous frequency of the 2P harmonic, and consequently the rotor speed. The black traces in Fig. 21b provide the 1P through 10P instantaneous frequencies as a function of time determined using this approach. It should be noted that while this approach provided a reasonable estimate of the rotor speed, it assumes that there is no lag between the change in rotor speed and resulting change in aerodynamic loads.

There are several features of note in the vertical hub force TFR and TnFR shown in Figs. 21b-21c. The first is the dominant 2P harmonic of the vertical hub force that shows a clear trend of increasing frequency and amplitude as a function of time. The 1P harmonic, which was absent during the 1500 RPM segment of the time history, appears in the TFR during the rotor speed increase, and never fully diminishes, even once the new constant rotor speed of 2500 RPM is reached at approximately 17 seconds. The 4P harmonic also becomes more prominent as the rotor speed begins to increase at approximately 1.8 seconds. A 6P harmonic can be seen throughout the entire time history. The 8P harmonic is not visible (low amplitude) in the first 6 seconds of the time history before abruptly increasing, followed by a reduction in amplitude to a final elevated value. Lastly, at two times in the time history, a temporary increase in amplitude centered about 295 Hz can be noted in the TFR at 2.4 and 6.1 seconds, first as the 10P and then 8P harmonics cross this frequency. These increases indicate that there is a mode whose frequency is independent of the rotor speed that responds to an excitation force at 295 Hz. Further investigation suggested that this mode is associated with the 6-DOF balance installed directly below the rotor to measure the rotor loads. Analysis of the DST amplitudes for the 295 Hz voice determined that the damping ratios of the 10P and 8P crossings were 0.29% and 0.14% critical. A further indication of the presence of this mode can be seen in the TFR (Fig. 21b) in the last four seconds of the time history, where the amplitude of the DST near 295 Hz periodically increases and decreases – an indication that there are two signals (the 295 Hz mode and, most likely, the 7P harmonic) close to each other in frequency. This same DST trend can be seen in the TFR of the analytical rotor model with elastic support structure where the modal frequency of the support structure and the rotor 2P harmonic were close to one another (see Figs. 11-13).

The rotor speed time history obtained from the experimental data in Fig. 21 was also used as an input to the CAMRAD II analysis of this single-rotor configuration. Three models of varying analytical complexity were analyzed: 1) a rigid-blade rotor on a rigid support structure, 2) a rigid-blade rotor on an elastic support structure, and 3) an elastic-blade rotor on an elastic support structure. All three cases utilized a free wake model since this aerodynamic model was shown to include the most higher-harmonic content, although the 2P amplitudes were previously shown to be significantly underpredicted (Table 2). The elastic blade, elastic support structure model (case 3) is not included in this discussion, since blade elasticity was shown to have a very limited effect on the rotor loads and support structure response for this particular rotor model.

The elastic support structure model in the previously-discussed parametric study consisted of a single mode with motion constrained to a single DOF. The MTB structure is significantly more complex, whose modeling is further complicated by the fact that the MTB is a reconfigurable testbed, allowing independent changes in the lateral and vertical placement, as well as shaft tilt, of the individual rotors. A ground vibration test (GVT) was not conducted on the exact configuration for which data is presented in Fig. 21, therefore, GVT data for the most similar configuration available were used to develop the modal representation of the rotor support structure. The modal model consists of 8 modes with translational DOFs in the vertical, lateral and

longitudinal directions – data on the rotational DOFs were not available, and therefore rotational DOFs were not included in the modal representation. To account for the differences between the tested configuration and the GVT configuration, engineering judgement was used to adjust the measured frequencies of the identified modes. The final frequencies of the modes included in the support structure model are 12, 20, 40, 60, 80, 170, and 270 Hz. The modal damping ratios for the first six modes were set to 0.5 percent critical and the two highest modes to 0.1 percent critical.

The vertical hub force time history and its TFR and TnFR for the rigid blade, rigid support structure model are presented in Fig. 22. The analytical force time history (blue line in Fig. 22a) also includes the time history of the rotor speed (in black), and the measured vertical hub force (gray) for comparison. The moving mean of the analytical model hub force follows the experimental data well, but the dynamic component of the force is significantly under predicted, as was expected.

The TFR and TnFR of the analytical vertical hub force are presented in Figs. 22b-22c, respectively. These figures are plotted using the same color intensity scale and time and frequency range to provide a direct comparison to the experimental data TFR and TnFR provided in Fig. 21b-21c. The TFR includes an overlay of traces indicating the instantaneous frequencies of the 1P through 10P harmonics. Qualitatively, the TFRs and TnFRs share many of the same

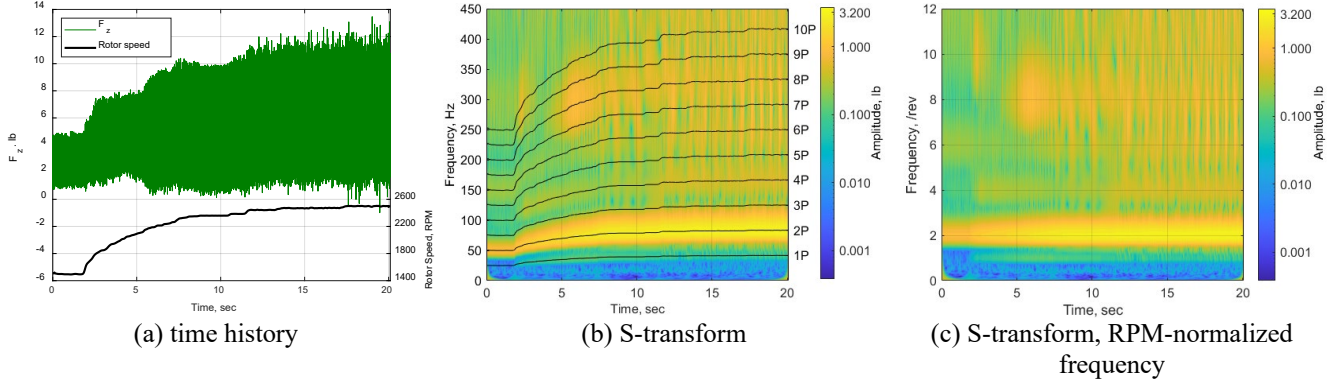


Figure 21. MTB vertical hub force during a 1000 RPM rotor speed change and its TFR and TnFR, $V=40$ ft/s, $\alpha_s = -2$ deg.

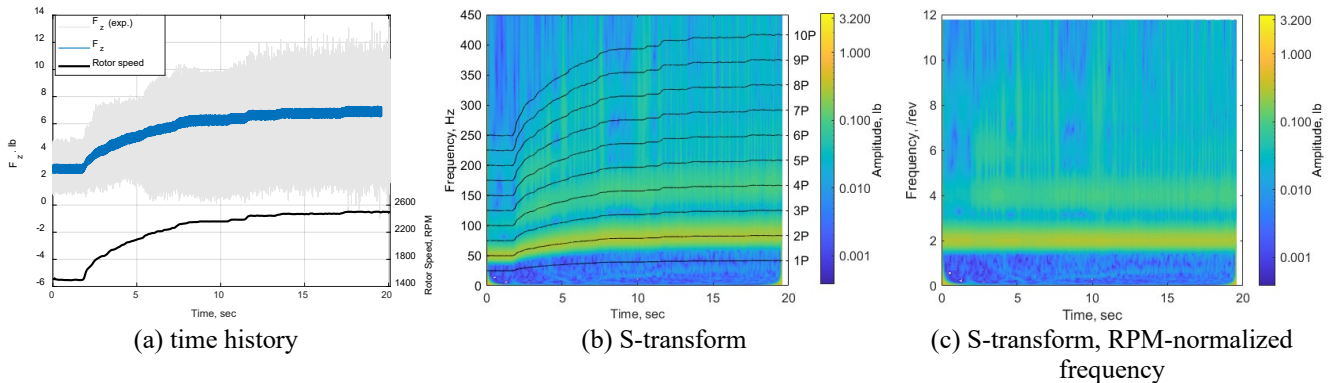


Figure 22. The vertical hub force and its TFR and TnFR, $V=40$ ft/s, $\alpha_s = -2$ deg; free wake, rigid fuselage, rigid blade.

features, although the analytical model amplitudes are smaller. The analytical model also lacks the 1P harmonic; also, the rigid support structure assumption precludes any possible modal interaction in the 295 Hz range (possibly associated with the 6-DOF balance installed directly below the rotor to measure the rotor loads).

The vertical hub force time history and its TFR and TnFR for the rigid blade, elastic support structure model are presented in Fig. 23. These figures look very similar to the rigid support structure model presented in Fig. 22. This similarity is best explained by an observation from the parametric study: the hub loads in this rotor model are almost entirely comprised of aerodynamic loads with small inertial components. This observation was corroborated by extracting the inertial component of the vertical hub force and examining the amplitude of its DST (not presented). Most of the inertial force frequency content was limited to the 2P harmonic and its interaction with the 60 and 80 Hz support structure modes.

A more quantitative comparison of the experimental and analytical hub loads can be made by extracting the 2P, through 10P voices from the TnFRs provided in Figs. 21c, 22c, and 23c. These harmonic amplitudes are compared in Figs. 24a-24e, where the experimental results are presented in green, rigid support structure analytical model results are in blue, and the elastic support structure analytical model results are presented in red; for reference, the rotor speed is included in Fig. 24f. As previously noted, the amplitudes of the hub force harmonics from both analytical models are an order of magnitude smaller than their experimental counterparts. The differences between the rigid and elastic support structure models are small enough that at the scale of Fig. 24, they appear almost identical. The most notable features of these harmonics are:

- The 2P hub force in the analytical models is insensitive to the rotor speed while the higher harmonics see an initial increase during the highest ramp-rate of the rotor speed (approx. 2-5 sec.)
- An increase in experimental 2P hub force coincides with the rotor speed increase.

- An increase in experimental 10P and 8P hub loads occurs at approximately 2.5 and 6.1 seconds, as those two harmonics pass through the 295 Hz mode. These increases are not expected to be present in either analytical model since the 295 Hz mode is currently not included in the analytical models. Further analysis of the elastic support

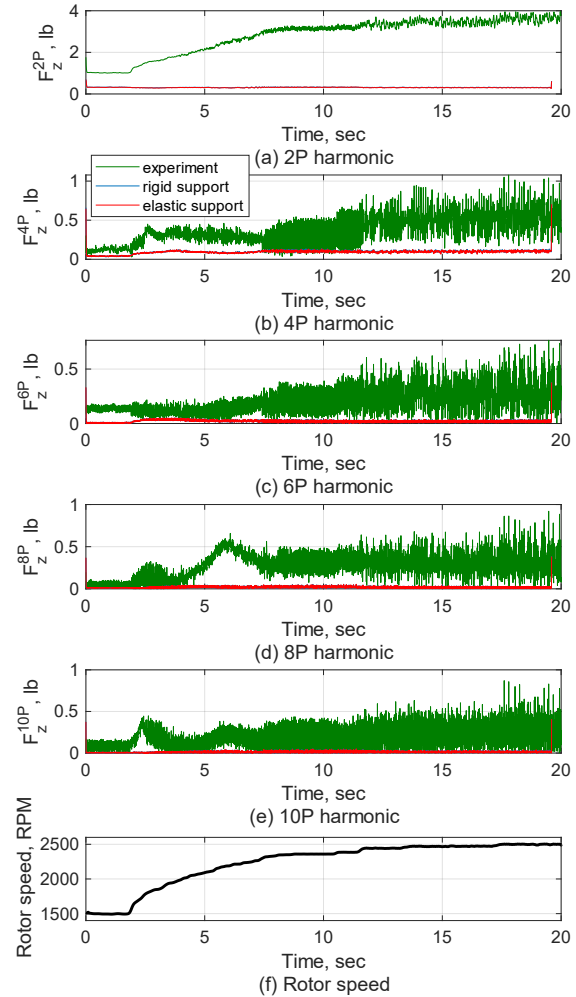


Figure 24. Amplitudes of experimental and analytical vertical hub force, 2P through 10P TnFR voices, $V=40$ ft/s, $\alpha_s = -2$ deg.

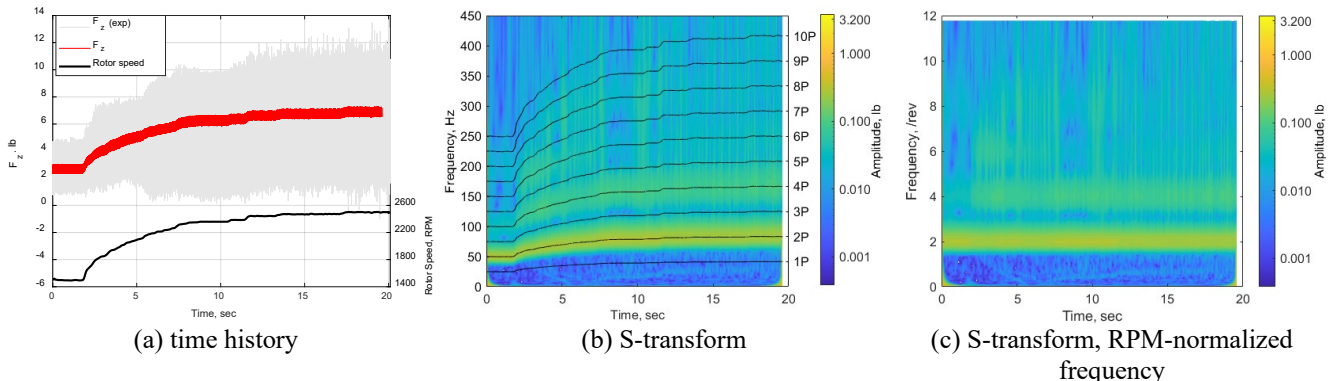


Figure 23. The vertical hub force and its TFR and TnFR, $V=40$ ft/s, $\alpha_s = -2$ deg; free wake, elastic fuselage, rigid blade.

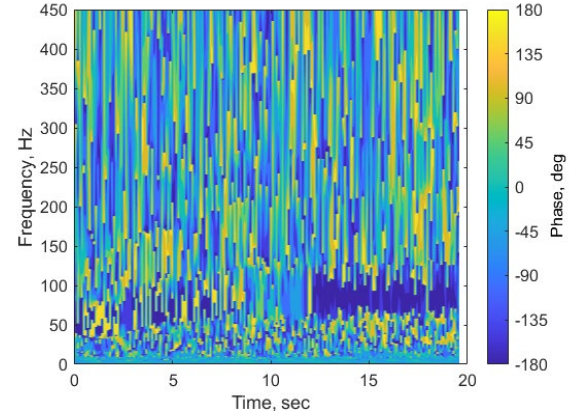
structure model suggested that the aerodynamic forces in this frequency range were too small to excite the support structure in a meaningful way (not presented).

The vertical component of the elastic support structure response measured at the hub of the analytical model is provided in Fig. 25a. The moving mean of the support structure response corresponds the changes in the rotor speed since thrust is directly related to rotor speed. There appear to be several segments of the time history where the dynamic response increases. The most prominent of these increases occurs between 14 and 17 seconds in Fig. 25a. This increase in the dynamic response is more clearly visible in Fig. 25b, the TFR of the displacements, where low (less than 1P) frequency content and 2P content are clearly discernable. Above 150 Hz, the frequency content is much more limited. Figure 25c focuses on the lower frequency range of the TFR and includes lines to highlight the frequencies of the first 6 support structure modes. In this figure, the excitation of the 12, 20 and 25 Hz support structure modes is clearly visible. Also of note is the crossing of the 2P harmonic with the 60 Hz mode (5th mode, labeled $m_f=5$) at approximately 2.5 seconds. This event results in an increase in the 2P response of the support structure that does not dissipate for another 5 seconds. Finally, at approximately 11.5 seconds, the 6th structural support mode (labeled $m_f=6$) is crossed by the 2P harmonic causing an increase in the 2P response. Due to the proximity of the 2P harmonic (approx. 83 Hz) to the 6th structural support mode (80 Hz), the 2P response remains elevated for the remainder of the time history. This dynamic behavior is an example of the complex interactions associated with varying RPM applications compared to the constant RPM applications (discussed earlier in the Introduction section).

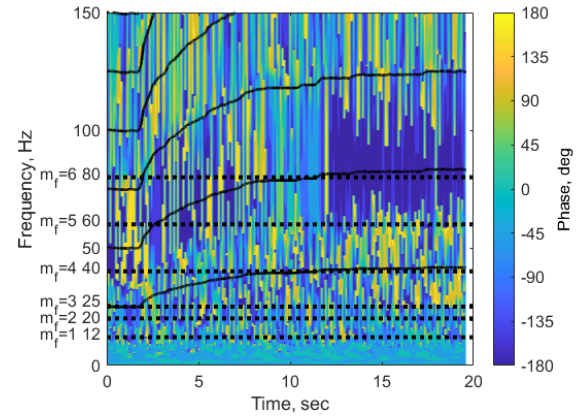
The phase between the aerodynamic component of the hub force and the support structure response was calculated by performing a localized cross-spectral analysis using the DST. The TFR of the phase determined by this cross-spectral analysis is provided in Fig. 26a. The prominent feature of this TFR is the constant-phase region starting at 12 seconds that is centered at a frequency of approximately 80 Hz. Fig. 26b provides the same phase TFR, but for a smaller frequency range, with an overlay of rotor speed harmonics (solid black lines) and support structure modal frequencies (dotted black lines). This figure suggests that the region of constant phase

is due to the proximity of the 2P harmonic and the 80 Hz support structure mode.

While the phase TFR provides a high-level overview of the interaction between the aerodynamic force and the hub vertical response, the nature of the interaction becomes more evident by simultaneously examining the voice amplitudes of the hub force (Fig. 24b) and the hub displacement (Fig. 25b), and the phase from Fig. 26 at the modal frequencies of the support structure model. For brevity, a more detailed discussion will focus on the 80 Hz mode (mode 6, labeled $m_f=6$ in Fig. 26b). The force and displacement amplitudes

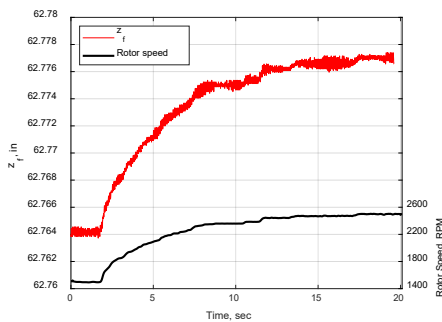


(a) S-transform

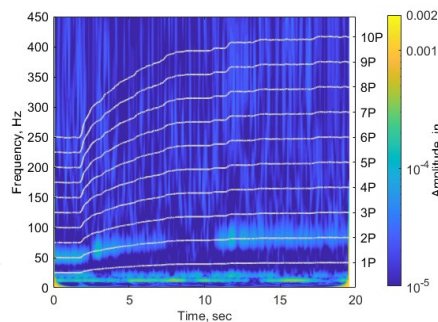


(b) S-transform, lower frequency detail

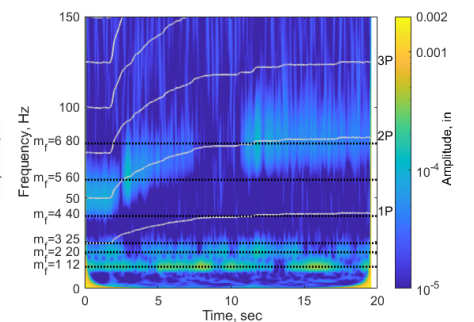
Figure 26. Phase of hub response relative to aerodynamic forcing, $V=40$ ft/s, $\alpha_s = -2$ deg; rigid rotor, elastic support structure.



(a) time history



(b) S-transform



(c) S-transform, lower frequency detail

Figure 25. Support structure response and its TFR, $V=40$ ft/s, $\alpha_s = -2$ deg; rigid rotor, elastic support structure.

and phase at 80 Hz is provided in Fig. 27a. The 2P harmonic frequency as a function of time is provided in Fig. 27b. The 2P harmonic passes through 80 Hz at 11.5 seconds (highlighted in Fig. 27a) and eventually reaches a final frequency of 83.3 Hz – corresponding to the ending rotor speed of 2500 RPM.

The 80 Hz voice amplitude of the hub force (red line, Fig. 27a) appears to correspond to the increase in the 2P frequency. The vertical hub displacement (blue line) shows an increase in amplitude, starting around 10 seconds, as the 2P harmonic approaches 80 Hz at 11.5 seconds. The maximum displacement amplitude lags this frequency coalescence, but this increase in hub motion is not reflected in the hub force time history (red) due to the relative size of the aerodynamic and inertial loads (comparison not presented). Because the 2P harmonic approaches and passes through this modal frequency relatively slowly, the modal response has the time to react to the aerodynamic forcing, resulting in an initial phase “lock in” such that the hub response is in-phase with the aerodynamic forcing starting at approximately 10 seconds, followed by a shift to -180 degrees after passing through resonance at 11.5 seconds.

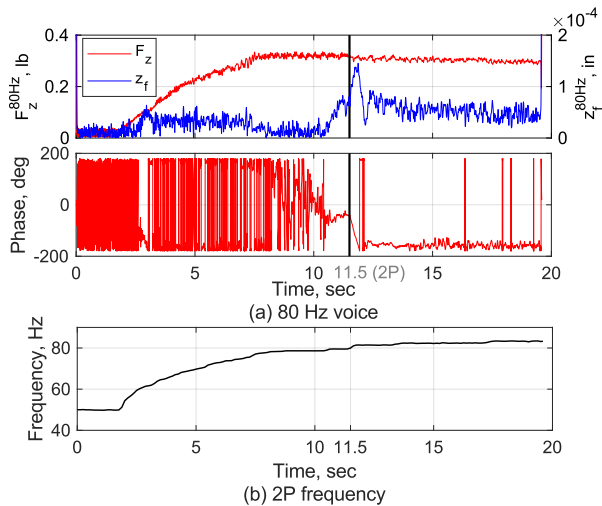


Figure 27. Amplitude of vertical hub force and displacement at the frequency 6th mode of the support structure, $V=40$ ft/s, $\alpha_s = -2$ deg; rigid rotor, elastic support structure.

CONCLUSIONS

A two-part analytical study was conducted to examine how modeling choices affect the dynamic rotor thrust of a two-bladed, small-scale rotor undergoing a change in rotor speed in a wind-tunnel setting. The comprehensive aeroelastic rotorcraft analysis software CAMRAD II was used to model a 24.5-inch diameter, 2-bladed rotor tested during the 2019 wind-tunnel entry of the NASA Multirotor Test Bed (MTB). Throughout this analysis, the following test condition from the above wind-tunnel entry was considered: free stream velocity of 40 ft/s, a shaft angle of -2 deg. (nose-down), and a starting and ending rotor speed of 1500 RPM ($\mu = 0.250$) and

2500 RPM ($\mu = 0.150$), respectively. Unlike traditional analytical solutions that enforce periodicity, this study utilized a time-marching solution to model the rotor undergoing a rotational speed change.

The analytical model was first used in a parametric study to understand how the rotor transient response is affected by the choice of rotor wake model, blade elasticity, and inclusion of a single degree-of-freedom (DOF) elastic support structure model tuned to pass through resonance during the rotor speed change. The second part of the study utilized these results to appropriately model a single-rotor configuration of the MTB undergoing a 1000-RPM rotor speed change.

In this study, the rotor speed varied as a function of time, so the resulting solutions were nonstationary – the frequency content changed as a function of time – and therefore analyses using traditional Fourier transform signal processing methods may not be appropriate. In place of the Fourier transform, an alternate signal analysis method called a Stockwell transform, or S-transform, was employed. The S-transform was used to extract the time-varying frequency content of the rotor thrust and hub displacement for the various analytical models. The results of these analyses allowed the comparison of time-varying signal amplitudes at specific frequencies (or rotor harmonics), whose frequencies varied with rotor speed. The S-transform was also used to determine the damping of the rotor system as well as the time and frequency varying phase between the aerodynamic rotor force and the response of the elastic rotor support structure. Finally, the S-transform was utilized to determine the time-dependent frequency of the 2P harmonic from the wind-tunnel data, which was then used to develop a rotor speed time history utilized in the CAMRAD II model of the experiment.

The major findings from the analytical parametric study of a rotor undergoing a rotor speed change include:

- The uniform inflow model did not produce rotor thrust frequency content higher than the blade passage frequency of the rotor.
- The dynamic inflow model required 55 states for convergence of the rotor thrust. It produced the largest 2P thrust that increased in amplitude as a function of rotor speed. The model also resulted in 4P rotor hub loads that decreased with increasing rotor speed.
- The free wake model utilized in this study resulted in the smallest dynamic vertical hub force of all the aerodynamic models tested. The amplitude of the 2P harmonic was insensitive to the change in rotor speed, while the 4P harmonic amplitude increased with rotor speed. The free wake model also produced frequency content at 6P during the rotor speed change portion of the time history.
- The current small-scale rotor blades (KDE-CF245) are extremely stiff, and the inclusion of blade elasticity in the model produced negligible changes in the rotor vertical hub force.

- The single DOF elastic support structure model had a significant effect on the vertical rotor hub force, primarily due to changes in the inertial component of this force. The choice of inflow model affected the amplitude of the rotor response where the dynamic inflow produced the largest response, while the free wake model produced the smallest response. The time-marching solution shows that the peak unsteady thrust amplitude lags the frequency coalescence between the 2P harmonic and the support structure mode, whereas the periodic solution predicts a significantly higher maximum response that occurs at the resonance frequency.
- The phase difference between the thrust and the hub motion of the periodic solutions followed a classic steady-state solution of a 1-DOF forced mass-spring-damper system, shifting from 0 degrees (in-phase) to -180 degrees (out of phase) in a manner consistent with a lightly-damped system (damping provided by the aerodynamic model). The phase of the time-marching solution continued to change even after the final rotor speed was reached, finally settling at -180 degrees once the transient hub motion decayed.

Comparison of the MTB experimental and the analytical model data showed that:

- The Stockwell transform of the experimental rotor thrust identified the 1P, 2P, 4P, 6P, and 8P harmonic content, each affected by the change in rotor speed. Additionally, a rotor-support structure coupled response was identified affecting the 8P and 10P rotor thrust harmonics as they passed through 295 Hz. This frequency was associated with a balance located directly below the rotor used to measure the hub forces and moments.
- The analytical model employing a free wake was selected to model the wind tunnel test condition. The computed vibratory rotor thrust was significantly lower than the measured vibratory thrust but included most of the same frequency content and followed the same trends as the experiment. The analytical model did not predict the high-frequency rotor-support structure interaction, due to the small rotor thrust amplitudes at the 8P and 10P harmonics.

Author contact:

Martin K. Sekula, martin.k.sekula@nasa.gov

Carl R. Russell, carl.r.russell@nasa.gov

ACKNOWLEDGMENTS

The authors would like to thank Dr. Craig Streett from NASA Langley for many discussions on nonstationary signal processing; Dr. Wayne Johnson from NASA Ames for his assistance in setting up the rotor speed variation modifications to the CAMRAD II model; and Mr. Matthew Wilbur, Dr. Robert Thornburgh and Mr. Andrew Kreshock from the Army Research Laboratory and Dr. Preston Martin from the U.S.

Army Research, Development, and Engineering Command for many insightful discussions on the subject of this work.

REFERENCES

1. Staruk, W., Butt, L., Hennig, G., Bonny, E., Gary, C., Represa, D., and Toner, R., "Wind Tunnel Testing and Analysis of a Rigid, Variable Speed Rotor for eVTOL Applications," Vertical Flight Society's 76th Annual Forum and Technology Display, Virtual, Oct. 6-8, 2020.
2. Lei, Y. and Cheng, M., "Aerodynamic Performance of Hex-Rotor UAV considering the Horizontal Airflow," *Applied Science*, 9, 4797, 2019; doi:10.3390/app9224797
3. Bowen-Davies, G. and Chopra, I., "Aeromechanics of a Slowed Rotor," 56th AIAA/ASCE/AHS/ASC Structures, Structural Dynamics, and Materials Conference, AIAA 2015-0951, 5-9 January 2015, Kissimmee, Florida, doi: 10.2514/6.2015-0951
4. Amri, H., Feil, R., Hajek, M., and Weigand, M., "Possibilities and Difficulties for Rotorcraft using Variable Transmission Drive Trains," *CEAS Aeronautical Journal* (2016) 7:333–344, doi: 10.1007/s13272-016-0191-6
5. Zhang, J., Smith, E. C., and Zajacowski, F., "Analysis of Rotor Start-Up and Shutdown on a Sea-Based Oil Rig," *Journal of Aircraft*, vol. 54, no. 1, January-February, 2017. doi: 10.2514/1.C033467
6. Keller, J. A., and Smith, E. C., "Analysis and Control of the Transient Shipboard Engagement Behavior of Rotor Systems," *Proceedings of the AHS 55th Annual Forum*, AHS International, Alexandria, VA, May 1999, pp. 1064–1078.
7. Mortimer, P., Johnson, C., Sirohi, J., Platzer, S., and Rauleder, J., "Experimental and Numerical Investigation of a Variable-Speed Rotor for Thrust Control," *Proceedings of AIAA AVIATION 2020 Forum*, AIAA 2020-2791, virtual event, June 15-19, 2020. doi: doi.org/10.2514/6.2020-2791
8. Chandrasekaran, R. and Hodges, D. H., "Performance Advantages and Resonance Analysis of a Variable Speed Rotor Using Geometrically Exact Beam Formulations," *Proceedings of the 77th Annual Forum of the VFS*, paper 77-2021-0076, virtual event, May 2021.
9. Bauschau, O. A., "DYMORE User's Manual," DymoreSolutions, 2020.
10. Johnson, W., "Technology Drivers in the Development of CAMRAD II," *American Helicopter Society Aeromechanics Specialist Meeting*, San Francisco, CA, January 19–21, 1994.
11. Hammond, J. K. and White, P. R., "The Analysis of Non-Stationary Signals using Time-Frequency Methods," *Journal of Sound and Vibration*, (1996) **190**(3), 419-447, doi: 10.1006/jsvi.1996.0072

12. Torrence, C. and Compo, G. P. "A Practical Guide to Wavelet Analysis," Bulletin of the American Meteorological Society, vol. 79, no. 1, pp 61-78, Jan 1998, doi: 10.1175/1520-0477.1998.079
13. Stockwell, R. G., "Why Use the S-Transform," Fields Institute Communications, v 52, 2007, 279-309. doi: 10.1090/fic/052/13
14. Stockwell, R. G., Mansinha, L., and Lowe, R. P., "Localization of the Complex Spectrum: The S-Transform," IEEE Transactions on Signal Processing, vol 44, no.4 April 1996.
15. Bjarnason, T. A., Drabycz, S., Adler, D. H., Cairncross, J. G., and Mitchell, J. R., "Applying the S-Transform to Magnetic Resonance Imaging Texture Analysis," Fields Institute Communications, v 52, 2007, 311-322. doi: 10.1090/fic/052/13
16. Khare, S. K., Nishad, A., Upadhyay, A., and Bajaj, V., "Classification of emotions from EEG signals using time-order representation based on the S-transform and convolutional neural network," Current Trends in Cognitive Science and Brain Computing Research and Applications, v. 56, issue 25, Dec 2020, pp 1359-1361. doi: 10.1049/el.2020.2380
17. Cui, X. Z., and Hong, H. P., "Use of Discrete Orthonormal S-Transform to Simulate Earthquake Ground Motions," Bulletin of the Seismological Society of America, (2020) 110 (2): pp 565-575. doi: 10.1785/0120190212
18. Clapson, A., Barsuglia, M., Bizouard, M., Brisson, V., Cavalier, F., Davier, M., Hello, P., Kreckelberg, S., and Varvella, M., "A gravitational wave burst search method based on the S-Transform," Classical and Quantum Gravity, vol. 22, no. 18, Sept 2005, pp S1381-S1390. doi: 10.1088/0264-9381/22/18/S51
19. Russell, C. and Conley S., "The Multirotor Test Bed – A New NASA Capability for Advanced VTOL Rotorcraft Configurations," Proceedings of the 76th Annual Forum of the VFS, paper 76-2020-0356, virtual event, Oct. 2020.
20. Russell, C. and Sekula, M., "Comprehensive Analysis Modeling of Small-Scale UAS Rotors," AHS International 73rd Annual Forum, Fort Worth, TX, May 9-11, 2017.
21. Drela, M., "XFOIL: An analysis and design system for low Reynolds number airfoils," *Low Reynolds Number Aerodynamics*, Lecture Notes in Engineering, No. 54, Springer-Verlag, June 1989
22. Young, L.A., "Vortex Core Size in the Rotor Near-Wake," NASA TM 2003-212275, June 2003.
23. Ho, J. C. and Yeo, H., "Considerations in the Selection of Inflow States with Finite-State Dynamic Inflow," AIAA Journal, vol. 59, No 7. July 2021. doi: 10.2514/1.J060176
24. Stockwell, R. G., "A basis for efficient Representation of the S-transform," Digital Signal Processing, 17 (2007) p271-393. doi:10.1016/j.dsp.2006.04.006